https://doi.org/10.5194/egusphere-2026-880
Preprint. Discussion started: 13 April 2026

Contrasting land carbon uptake responses to El Niño–Southern Oscillation across North America

Wu Sun[1], Kelsey T. Foster[1,2], Yoichi P. Shiga[3], Julian Merder[1], Nina A. Randazzo[4,5], and Anna M. Michalak[1,2]

[1]Department of Global Ecology, Carnegie Institution for Science, Stanford, California, USA
[2]Department of Earth System Science, Doerr School of Sustainability, Stanford University, Stanford, California, USA
[3]Independent Researcher, San Francisco, California, USA
[4]Global Modeling and Assimilation Office, NASA Goddard Space Flight Center, Greenbelt, Maryland, USA
[5]Earth System Science Interdisciplinary Center, University of Maryland, College Park, Maryland, USA

Correspondence: Wu Sun (wsun@carnegiescience.edu)

Abstract. El Niño–Southern Oscillation (ENSO) drives year-to-year variability in the land carbon sink. While responses of land carbon uptake to ENSO have been documented at aggregated continental scales over North America, these responses arise from ENSO's climate impacts that vary across subcontinental regions. Disentangling diverse regional responses is crucial for attributing ENSO's impacts on carbon uptake to climatic drivers. Here, we characterize ENSO-driven carbon–climate interactions across North America, a data-rich continent with prominent responses to ENSO, by leveraging fine-resolution ($1^\circ \times 1^\circ$) top-down estimates of land carbon fluxes derived from tall-tower atmospheric CO_2 observations and spaceborne chlorophyll fluorescence measurements. We identify regions with distinct ENSO responses in the timing, direction, and magnitude of carbon uptake anomalies. Notably, regions where El Niño boosts carbon uptake, including the Pacific–Mountainous West and subtropical lands, are consistent with ENSO-driven shifts in the position of the subtropical jet. We further uncover contrasting patterns in how energy and water limitations mediate ENSO's impacts on carbon uptake across regions. These findings reveal key regional mechanisms connecting ENSO-driven climate variability with continental-scale carbon uptake responses and highlight the need to reassess tropical carbon–climate feedbacks in light of compensatory extratropical responses.

1 Introduction

El Niño–Southern Oscillation (ENSO) has far-reaching impacts on the global carbon cycle beyond the equatorial Pacific where it originates (Bacastow, 1976; Keeling et al., 1995; Jones et al., 2001; Fang et al., 2017; Liu et al., 2017; Bastos et al., 2018; Betts et al., 2020; Liu et al., 2024). El Niño, the warm phase of ENSO, leads to widespread warm and dry anomalies over the tropics (Trenberth et al., 1998), which suppress photosynthesis in the Amazon rainforest (Liu et al., 2017; Luo et al., 2018; Koren et al., 2018; Chen et al., 2024), amplify respiratory release of carbon in the African rainforest (Liu et al., 2017), and spark peatland fires in Indonesia and forest fires in the Amazon (Page et al., 2002; Chen et al., 2017). These planetary-scale impacts of ENSO on the terrestrial carbon cycle give rise to a striking relationship between tropical temperatures and atmospheric CO_2 growth rates (Jones and Cox, 2005; Cox et al., 2013; Wang et al., 2013, 2014), which has been used to constrain the sensitivity of tropical land carbon stocks to warming (Cox et al., 2013). Notably, extreme El Niño events markedly intensify the carbon cycle's sensitivity to tropical temperature anomalies (Li et al., 2024), fueling new interest in ENSO's carbon cycle impacts.

Less well understood are ENSO's impacts on the carbon cycle in extratropical lands, which have recently been shown to be globally significant (Hu et al., 2019; Liu et al., 2024). Contrary to tropical responses, for example, North America shows enhanced terrestrial net carbon uptake during El Niño (Hu et al., 2019), with an ENSO composite anomaly (El Niño − La Niña; $\sim 0.7\,\mathrm{Pg\,C\,yr^{-1}}$) comparable to the reduction of net carbon uptake over the Amazon ($0.9\,\mathrm{Pg\,C\,yr^{-1}}$) (Liu et al., 2017). How this unexpectedly strong response of the North American land carbon sink arises from ENSO's climate impacts remains underexplored.

ENSO shapes North American climate variability by modulating large-scale pressure anomalies and the jet stream's position over the Pacific–North American sector (Bjerknes, 1969; Horel and Wallace, 1981; Held et al., 1989; Trenberth et al., 1998; Seager et al., 2005). During El Niño, the Pacific subtropical jet typically shifts southward and extends eastward to the North American continent, enhancing the positive phase of the Pacific–North American pattern with stronger Aleutian Low and Canadian High. This pattern is typically associated with warmer conditions in northwestern North America, drier conditions in the Midwest, and wetter conditions from southern California to Florida in winter (Trenberth et al., 1998; Deser et al., 2018). Conversely, during La Niña, the Pacific jet stream shifts poleward, enhancing the blocking North Pacific High and leading to a more meandering polar jet stream. This pattern usually leads to colder and wetter conditions in midlatitude North America and drier conditions in subtropical North America in winter.

These ENSO-driven climate anomalies lead to cascading impacts on the North American carbon cycle, as illustrated by remotely sensed vegetation indicators (Bastos et al., 2013; Dannenberg et al., 2015, 2018; Luo et al., 2018; Zhang et al., 2019b; Du et al., 2021; Dannenberg and Johnston, 2023) and top-down carbon flux estimates (Rödenbeck et al., 2018; Hu et al., 2019; Liu et al., 2024). El Niño is generally associated with increased photosynthesis and net primary productivity relative to La Niña in southeastern temperate forests, subtropical drylands, and western North America (Bastos et al., 2013; Parazoo et al., 2015; Luo et al., 2018; Zhang et al., 2019b); however, the exact patterns may differ between El Niño types (Dannenberg and Johnston, 2023). El Niño also advances and prolongs the growing season in western North American biomes (Dannenberg et al., 2015, 2018; Dannenberg and Johnston, 2023). While there is limited understanding of ENSO impacts on respiration, terrestrial biosphere models suggest partial compensation between respiration and photosynthesis in response to ENSO based on predicted weaker responses in net carbon uptake than in photosynthesis (Parazoo et al., 2015; Dannenberg et al., 2021). In the absence of unprecedented large fires (e.g., the 2023 Canadian wildfire; Byrne et al., 2024), ENSO impacts on North American fire emissions are insignificant relative to impacts on photosynthesis and respiration, even for extreme El Niño events, such as the 1997 and 2015 El Niño (van der Werf et al., 2004; Burton et al., 2020). Combined, these responses translate to increased net carbon uptake over most of western North America during El Niño (Rödenbeck et al., 2018; Hu et al., 2019). A distinct feature of the North American carbon cycle's response to climate variability is a contrast between the humid east and arid west (Qian et al., 2008; Byrne et al., 2020), which was observed in the 2021 La Niña response (Liu et al., 2024).

Despite the notion that El Niño boosts the integrated North American land carbon sink and previous insights into certain regional responses, we lack a coherent understanding of the responses of North American land carbon uptake to ENSO, particularly concerning how these responses arise from ENSO's climate impacts, which vary across North American regions. Moreover, most prior studies have relied on remotely sensed vegetation indices and gross or net productivity estimated from them, which are not direct measures of net carbon balance. The few studies that have leveraged atmospheric CO_2 concentration observations to constrain carbon flux variability resulting from ENSO (Rödenbeck et al., 2018; Hu et al., 2019; Liu et al., 2024) have focused primarily on net continental-scale impacts. Given the diverse, region-specific impacts of ENSO on North American climate (Trenberth et al., 1998; Deser et al., 2018), we anticipate diverse, region-specific responses in net carbon uptake as well. Specifically, we hypothesize that El Niño leads to enhanced net carbon uptake in western and subtropical North America based on known ENSO-led hydroclimatic anomalies in these regions (Kurtzman and Scanlon, 2007; Deser et al., 2018).

Here, we use constraints provided by atmospheric CO_2 concentration measurements to advance an observationally-informed understanding of ENSO impacts on North American land carbon uptake. This "top-down" view also complements earlier "bottom-up" studies that leverage mechanistic understanding of underlying processes but are not informed by empirical constraints at regional scales. Specifically, we map ENSO impacts on North American land carbon uptake at fine regional scales by identifying regions sensitive to ENSO influences, examining the timing, direction, and magnitude of region-specific ENSO impacts, and attributing these impacts to specific climate anomalies. To do so, we use 96,000 CO_2 observations from 61 towers across North America (Fig. S1 and Table S1 in the Supplement) to derive geostatistical inverse model estimates of North American land carbon uptake at $1^\circ \times 1^\circ$ spatial and three-hourly temporal resolution during 2007–2015 and aggregate them *a posteriori* to monthly estimates. We leverage remotely sensed solar-induced chlorophyll fluorescence (SIF), a key indicator of the space-time patterns of photosynthesis (Frankenberg et al., 2011; Joiner et al., 2011, 2013; Guanter et al., 2014; Sun et al., 2017; Porcar-Castell et al., 2021), and reanalysis climate drivers to explain a portion of the space-time variability in CO_2 observations. This approach obviates the need for prior flux estimates from specific bottom-up models and therefore avoids the risk of prescribing the assumptions or parameterizations inherent to a certain terrestrial biosphere model. Using a clustering approach, we then identify regions where net carbon uptake shows a robust and coherent response to ENSO and examine regional responses in relation to ENSO phases. Next, we use generalized linear models and statistical model selection to attribute net carbon uptake anomalies to ENSO-related local climate anomalies for each region. We glean from these results an understanding of how ENSO-driven circulation changes, terrestrial aridity gradients, and local climate variability give rise to contrasting responses of net carbon uptake to ENSO across regions in North America.

https://doi.org/10.5194/egusphere-2026-880
Preprint. Discussion started: 13 April 2026

2 Methods

2.1 Atmospheric CO_2 observations

We obtain in situ measurements of atmospheric CO_2 mixing ratios from the ObsPack CO_2 GLOBALVIEWplus v3.2 data product provided by the National Oceanic and Atmospheric Administration (NOAA) Global Monitoring Laboratory (Masarie et al., 2014; Cooperative Global Atmospheric Data Integration Project, 2017). From 61 non-urban continuous-monitoring stations across North America (Fig. S1 and Table S1), we extract ~96,000 three-hourly averaged mid-afternoon CO_2 measurements (Table S2) following established data filtering practices in regional inverse modeling (Göckede et al., 2010; Gourdji et al., 2012; Fang and Michalak, 2015; Shiga et al., 2018b; Sun et al., 2021). The use of mid-afternoon CO_2 observations helps reduce transport errors as the boundary layer is usually well mixed during this time of the day. The filtering eliminates data that do not represent mesoscale flux variability by removing outliers, low-quality data (according to ObsPack quality flags), data that exceed background values by more than 30 ppm, ocean-influenced data, and data potentially affected by transport issues (Fang et al., 2014; Shiga et al., 2018b; Sun et al., 2021). To calculate biospheric CO_2 drawdowns or enhancements for inverse modeling, we subtract background values derived from interpolating marine boundary layer and free troposphere observations (same as the empirical background method in Hu et al., 2019) and also fossil fuel enhancements estimated from the Fossil Fuel Data Assimilation System (FFDAS) v2 emission inventory (Asefi-Najafabady et al., 2014). Overall, CO_2 data processing is consistent with Shiga et al. (2018b) and Sun et al. (2021).

2.2 Atmospheric transport

We use transport footprints from high-resolution Weather Research and Forecasting–Stochastic Time-Inverted Lagrangian Transport (WRF–STILT) model runs (10 km for temperate North America and 40 km for tropical and boreal North America) produced by the CarbonTracker-Lagrange project (https://gml.noaa.gov/ccgg/carbontracker-lagrange/) (Hu et al., 2019) to link observed CO_2 drawdowns or enhancements with surface fluxes in upwind regions (Lin et al., 2003; Skamarock and Klemp, 2008; Nehrkorn et al., 2010). The transport footprints are aggregated at $1^\circ \times 1^\circ$ spatial resolution and three-hourly temporal resolution for inverse model estimation of fluxes. Mean transport errors associated with the WRF–STILT footprints have been shown to be no greater than 0.15 ppm for CO_2, comparable to in situ measurement uncertainty (Rastogi et al., 2021).

2.3 Explanatory variables for inverse flux estimation

We use remotely sensed solar-induced chlorophyll fluorescence (SIF) and reanalysis climate drivers as covariates to explain a portion of the space-time variability in net carbon fluxes (Shiga et al., 2018b). Contiguous 15- or 16-day composite SIF maps are obtained from spatiotemporal kriging (Tadić et al., 2017) of Level 2 daily SIF estimates (v26) from the Global Ozone Monitoring Experiment 2 (GOME-2) instrument onboard the MetOp-A satellite (Joiner et al., 2013). In addition, we select a parsimonious set of monthly climate variables (see Sect. 2.4 Geostatistical inverse modeling) from the

https://doi.org/10.5194/egusphere-2026-880
Preprint. Discussion started: 13 April 2026

North American Regional Reanalysis (NARR) (Mesinger et al., 2006) to explain an additional portion of variability in net carbon fluxes. NARR variables considered in the model selection include accumulated precipitation ($\mathrm{kg\,m^{-2}}$), canopy conductance ($\mathrm{m\,s^{-1}}$), downward shortwave radiation ($\mathrm{W\,m^{-2}}$), evapotranspiration ($\mathrm{kg\,m^{-2}}$), potential evapotranspiration ($\mathrm{kg\,m^{-2}}$), precipitation rate ($\mathrm{kg\,m^{-2}\,s^{-1}}$), relative humidity (%), specific humidity ($\mathrm{kg\,kg^{-1}}$), air temperature at 2 m (K), snow cover (%), snow depth (m), and soil moisture ($\mathrm{kg\,m^{-2}}$). All variables are regridded to $1^\circ \times 1^\circ$ spatial resolution and repopulated at three-hourly temporal resolution to be compatible with transport footprints. We apply piecewise constant interpolation (monthly for climate drivers and every 15 or 16 days for SIF) in the temporal domain to avoid imposing an excessive constraint on sub-monthly variability in fluxes (Sun et al., 2021).

2.4 Geostatistical inverse modeling

We use geostatistical inverse modeling (GIM) to infer net biome exchange of CO_2 from atmospheric CO_2 concentration observations. Compared with typical Bayesian inversions that rely on prior information of flux estimates, the GIM approach is more directly informed by observations because it leverages a set of covariates to explain a portion of the variability in fluxes and an error covariance model to characterize deviation from the deterministic trend explained by these covariates (Michalak et al., 2004; Gourdji et al., 2010). Because GIM does not rely on explicit prior flux estimates from specific terrestrial biosphere models, it avoids the use of assumptions and parameterizations that vary across terrestrial biosphere models and that could bias posterior estimates. The approach follows established practices (Gourdji et al., 2012; Miller et al., 2018; Shiga et al., 2018b) and is briefly described here. More implementation details are given in Appendix A.

First, we use the Schwarz Bayesian information criterion (Schwarz, 1978) to select a parsimonious set of explanatory variables to capture observed variability in biospheric CO_2 drawdowns or enhancements (Gourdji et al., 2012; Miller et al., 2018; Shiga et al., 2018b). The explanatory variables selected in this step are kriged GOME-2A SIF ($\mathrm{mW\,m^{-2}\,nm^{-1}\,sr^{-1}}$), specific humidity ($\mathrm{kg\,kg^{-1}}$), and the precipitation rate ($\mathrm{kg\,m^{-2}\,s^{-1}}$). See Table S3 for the estimated coefficients of the selected explanatory variables.

Second, we fit parameters that define the model–data mismatch covariance matrix ($\mathbf{R}$) and the prior flux covariance matrix ($\mathbf{Q}$). We assume that model–data mismatch errors are uncorrelated across 61 CO_2 monitoring sites and in time, which means that the model–data mismatch covariance matrix ($\mathbf{R}$) is diagonal (Mueller et al., 2008; Gourdji et al., 2010). The prior flux covariance matrix ($\mathbf{Q}$) characterizes the spatiotemporal autocorrelation in the stochastic component of the fluxes and is represented using an isotropic exponential decay covariance function (Michalak et al., 2004; Gourdji et al., 2010); see Appendix A for a detailed description and Tables S4–S6 for optimized parameters.

With the covariance matrices ($\mathbf{Q}$ and $\mathbf{R}$) specified, we solve for the posterior estimates of the fluxes from the geostatistical inverse linear system of equations (Michalak et al., 2004; Yadav and Michalak, 2013) at three-hourly temporal resolution. We then aggregate the flux estimates monthly. See Fig. S2 for the mean seasonal cycle of flux patterns during the study period (2007–2015) and Fig. S3 for a summary of posterior uncertainties in monthly flux estimates. Finally, we subtract mean seasonal patterns of NBP (Fig. S2) from the original NBP estimates to obtain NBP anomalies.

https://doi.org/10.5194/egusphere-2026-880
Preprint. Discussion started: 13 April 2026

In setting up the flux inversion, we did not pre-subtract influences from fire emissions following Hu et al. (2019). Instead, we filtered data for which the enhancement is more than 30 ppm above the background to mitigate near-field fire influences. As a result of this setup, the carbon flux estimates we obtain here fit the definition of net biome exchange (NBE), but differ from net ecosystem exchange (NEE) that excludes fire influences (Chapin et al., 2006; Hu et al., 2019; Byrne et al., 2023). See Fig. S4 for an examination of ENSO impacts on anomalies in North American fire emissions. For a comparison of net carbon uptake anomalies between our geostatistical inverse estimates and the CarbonTracker-Lagrange inverse estimates (Hu et al., 2019), see Fig. S5.

2.5 Carbon flux estimates from terrestrial biosphere models and an upscaled data product

For comparison, we also use the ensemble mean of 16 terrestrial biosphere models from the "Trends and drivers of the regional scale terrestrial sources and sinks of carbon dioxide" project version 11 (TRENDY v11) (Sitch et al., 2015, 2024; Friedlingstein et al., 2022) to examine how well terrestrial biosphere models represent ENSO impacts on carbon flux patterns. See Table S7 for a list of TRENDY v11 models. We use model simulations in the S3 scenario, which is forced by time-varying drivers of climate (CRUJRA v2.3) (Harris, 2022), CO_2, and land use as described in Sitch et al. (2024). All model output was harmonized at monthly temporal resolution and $1^\circ \times 1^\circ$ spatial resolution. Similarly, NBP anomalies were calculated from the FLUXCOM-X-BASE upscaled net ecosystem exchange (NEE) product (Nelson et al., 2024) and aggregated over the same North American domain.

2.6 ENSO indices and phase classification

We use a suite of ENSO indices to identify robust spatial patterns of the correlation between ENSO and NBP anomalies. The primary ENSO index we use is the Oceanic Niño Index (ONI) provided by the NOAA National Weather Service Climate Prediction Center (2024a). ONI represents the three-month running mean of sea surface temperature (SST) anomalies from the ERSST V5 reanalysis (Huang et al., 2017a, b) in the Niño 3.4 region (5 °N to 5 °S, 120 °W to 170 °W) relative to a rolling 30-year base period updated every five years (Lindsey, 2013). ONI values in the study period 2007–2015 are based on the 1991–2020 climatology. For comparison, we also use monthly Niño 3.4 SST anomalies from the HadISST v1.1 reanalysis (Rayner et al., 2003), and Southern Oscillation Index (SOI) from the University of East Anglia Climatic Research Unit (Ropelewski and Jones, 1987), both relative to the base period of 1981–2010. In addition, we use the Multivariate ENSO Index v2 (MEI v2) (Wolter and Timlin, 1993; Zhang et al., 2019a), which is based on the leading principal component time series of the standardized anomalies of sea level pressure, SST, and surface zonal and meridional winds, from JRA-55 reanalysis (Kobayashi et al., 2015), and outgoing longwave radiation (OLR), from NOAA Climate Data Records OLR v2.7 (Lee et al., 2018) during 1979–2018. These four ENSO indices—ONI, Niño 3.4 (HadISST), SOI, and MEI v2—are used to ensure consistency in the correlation patterns between ENSO and NBP anomalies.

We define ENSO phases based on ONI thresholds: El Niño is defined as ONI $\geq 0.5\,^\circ$C and La Niña is defined as ONI $\leq -0.5\,^\circ$C (McPhaden et al., 2006). Neutral conditions are defined by $-0.5\,^\circ\mathrm{C} < \mathrm{ONI} < 0.5\,^\circ\mathrm{C}$. Different ENSO indices are generally consistent in the major El Niño/La Niña events identified during the study period (Fig. S6).

As the Pacific–North American (PNA) pattern and the North Atlantic Oscillation (NAO) may interact with ENSO, we also use the PNA pattern index and the NAO index from the NOAA National Weather Service Climate Prediction Center (2024b) to examine their influences on North American terrestrial carbon uptake (Fig. S7).

2.7 Identification of ENSO-sensitive regions

We identify ENSO-sensitive regions based on the direction and statistical significance of lagged correlations between NBP anomalies and ENSO indices.

We first evaluate the spatial correlation patterns between NBP anomalies and four ENSO indices. We calculate the time lag that maximizes the absolute value of the cross-correlation between ENSO indices and NBP anomalies in each grid cell (Fig. S8) as well as the cross-correlation based on this optimal time lag (Fig. S9), for each of the four ENSO indices. In doing so, we assume that North American NBP anomalies are always synchronous to or lag behind ENSO indices due to the nature of atmospheric teleconnections (that is, the cause must exist prior to its effect) and that the time lag under consideration is between 0–11 months, i.e., less than one year.

We then filter grid cells for the strength of observational constraint and for consistency and robustness of the responses of NBP anomalies to ENSO (Fig. S10). We limit the analysis to the 80 % of grid cells to which the sensitivity of CO_2 observations to surface fluxes is strongest (Figs. S1 and S10a) to avoid interpreting fluxes and clusters in the least well constrained regions of the continent. For a grid cell to show a consistent response across four ENSO indices, we require that the optimal lagged correlations between NBP anomalies and MEI v2, Niño 3.4 (HadISST), and ONI (ERSSTv5) have the same sign and that this sign is opposite to that of the optimal lagged correlation between NBP anomalies and SOI (Fig. S10c), as SOI is defined with an opposite sign compared with other ENSO indices used here (Fig. S6). For robustness, we require that all optimal lagged correlations for a grid cell to be significant at $p < 0.05$ level (Fig. S10b).

We then use agglomerative clustering to organize the grid cells that meet observational representativeness, consistency, and robustness criteria (Fig. S10d) into geographically coherent clusters. To do so, we define a distance metric that combines both distances in space and time. For any pair of grid cells, the distance in space is defined as the orthodromic (great-circle) distance, bound between 0 and π, and the distance in time is defined as the sum of absolute differences between their time lags for each ENSO index. Given that the spatial domain is limited to North America (i.e., the orthodromic distance between two grid cells is typically much lower than π), we used a weight of two for the orthodromic distance in the combined distance in order to balance temporal and spatial terms and to suppress spatially highly discontinuous clusters. Grid cells are clustered based on the distance matrix using the agglomerative clustering function provided by Scikit-learn v1.4.2 (Pedregosa et al., 2011), using the average linkage function. To ensure that a region does not mix up grid cells that show ENSO responses in different directions, we separately cluster grid cells with positive and negative correlations between NBP anomalies and ONI (Fig. S10d). The number of clusters is adjusted to capture spatially distinct clusters with positive and negative NBP responses (Fig. S11). For interpretation, we name the identified ENSO-sensitive regions according to the major geographic regions they contain and their spatial centroids, though some clusters may include a small number of discontiguous grid cells with similar responses on the periphery of the cluster core, as the clustering approach is data-driven and region-agnostic.

2.8 ENSO composite differences

We evaluate ENSO composite differences, i.e., differences between El Niño and La Niña mean anomalies, at the grid cell level and for the identified ENSO-sensitive clusters following established practices (Deser et al., 2018) and with time lags considered. We also use a two-sided Welch's t-test to test the significance of ENSO composite differences.

2.9 Attribution of influences of local climate anomalies on carbon uptake anomalies

We investigate how net carbon uptake (i.e., NBP) anomalies in each ENSO-sensitive region are regulated by ENSO-driven anomalies in a set of potential climate drivers (Fang and Michalak, 2015). These climate variables include air temperature, shortwave radiation, precipitation rate, VPD, and soil moisture from the NARR data (Mesinger et al., 2006). We calculate the anomalies of these variables by subtracting mean seasonal cycles during 2007–2015 and convert them into Z-scores for the attribution.

We use the Schwarz Bayesian information criterion (Schwarz, 1978) to select among both synchronous and lagged relationships between local climate anomalies and NBP anomalies, with local climate anomalies leading NBP anomalies by up to three months. Although precipitation and specific humidity (which correlates with VPD) have already been used as covariates for the deterministic component of the GIM posterior flux estimates, these estimates also have a spatiotemporally correlated stochastic component constrained by atmospheric CO_2 observations (Michalak et al., 2004). Given that these observations provide sufficient constraint over temperate North America (Fig. S1) and that SIF, not precipitation or specific humidity, dominates the explained CO_2 variability (Shiga et al., 2018b), it is unlikely for NBP anomalies to be overly constrained by the covariates selected for the deterministic component of GIM. We also consider temporal autocorrelation in NBP anomalies with a lag between one and three months. We perform variable selection by fitting a generalized linear model using the "gamlss" package in R (Rigby and Stasinopoulos, 2005) and minimizing the Schwarz Bayesian information criterion. To avoid overfitting, we allow each climate anomaly to occur no more than once in the model regardless of its time lag (0–3 months). Moreover, we only allow combinations of climate anomalies that do not exhibit strong collinearity. This is achieved by dropping any model with a term associated with a variance inflation factor greater than five (Table S8). Throughout all temperate ENSO-sensitive regions, we find that a t-distribution best represents the conditional distribution of NBP anomalies. Model validation is done by examining normalized quantile residuals. We assess the relative importance of selected variables by ranking the absolute values of standardized coefficients for Z-scored climate anomalies. See Table S8 for the selected variables and standardized coefficients for each region.

We also test the robustness of selected explanatory variables by examining standardized coefficients from models that use only a subset of explanatory variables from the selected model. An explanatory variable has an uncertain influence on NBP anomalies, if its standardized coefficients change sign among these submodels tested. See Table S9 for the identified explanatory variables with uncertain influences.

For a subset of ENSO-sensitive regions that show inconsistent responses between local climate anomalies and NBP anomalies, we further examine seasonal influences of local climate anomalies on NBP anomalies by redoing the attribution for early (winter and spring, or December–May) and late seasons (summer and fall, or June–November). Standardized coefficients from this attribution analysis are shown in Table S10.

2.10 Identification of jet stream locations

We use the Manney et al. (2011) algorithm implemented in the Python package “jsmetrics” v0.2.7 (Keel et al., 2024; Keel, 2024) to identify latitudes of jet stream cores from daily NARR zonal and meridional winds at the 200 hPa pressure level (cf. Shaw and Miyawaki, 2023). We regrid NARR wind data to 1° × 1° spatial resolution, consistent with carbon flux estimates, before running the jet core identification algorithm. We focus on winter months (December, January, and February) when the Pacific jet stream is stronger than in other seasons. After identifying daily jet core locations, we pool together El Niño winters (2010 and 2015, including Decembers in previous years) and La Niña winters (2008, 2009, 2011, and 2012) to derive median latitudinal positions of the Pacific jet stream during El Niño and La Niña winters. For visualization purposes, the median latitudinal positions of the jet stream are smoothed using a Savitzky–Golay filter with an 11° longitudinal window to suppress smaller-scale variability.

3 Results

3.1 Spatial patterns of lagged ENSO impacts on regional net carbon uptake anomalies

While El Niño enhances the integrated North American carbon sink (Hu et al., 2019), we find a diversity of responses in terms of timing, magnitude, and direction across regions (Fig. 1). Results show that ENSO leads to lagged responses of net carbon uptake (i.e., NBP) anomalies that vary substantially across regions (Fig. 1a). The lagged impact is expected because ENSO elicits lagged responses in atmospheric circulation (Kumar and Hoerling, 2003; Su et al., 2005) and peak ENSO (boreal winter) precedes the North American growing season. Indeed, we find that NBP anomalies on the Pacific coast of North America and in the southeastern US generally lag ENSO indices by one season (Fig. 1a and Fig. S8). In contrast, NBP anomalies in central south and mid-continental regions lag ENSO indices by half a year or more (Fig. 1a and Fig. S8). These differences in the lag between NBP anomalies and ENSO (Fig. 1a) result from diverse teleconnected ENSO impacts on regional climate anomalies (Fig. S12). For example, temperature anomalies on the Pacific coast show a similar delay in response (0–2 months; Fig. S12a) to ENSO as do NBP anomalies there (Fig. 1a), whereas temperature anomalies (Fig. S12a) and NBP anomalies (Fig. 1a) in subtropical regions both lag behind ENSO by more than six months. Different peak carbon uptake months between the Pacific coast and southwestern North America (May) and other regions (June and July) also contribute to observed differences in lagged responses to ENSO (Fig. S13).

https://doi.org/10.5194/egusphere-2026-880
Preprint. Discussion started: 13 April 2026

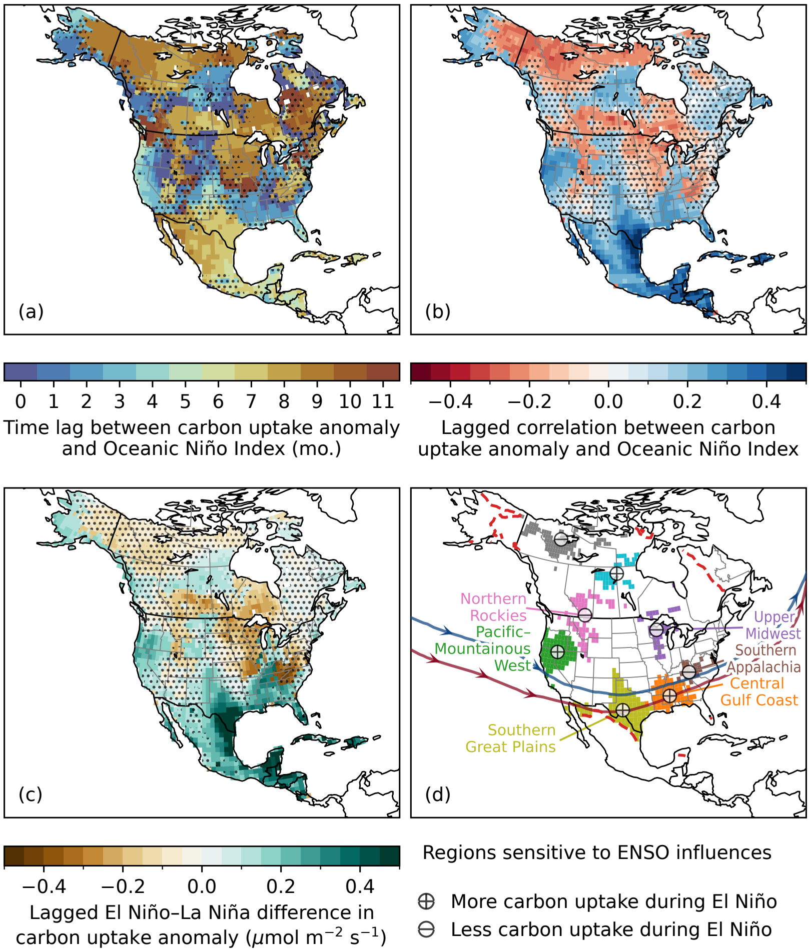

Figure 1. Spatial patterns of the lagged response of North American biospheric carbon uptake to ENSO. (**a**) Time lags between the anomaly in net carbon uptake (i.e., net biome productivity) and the Oceanic Niño Index (ONI) in months that maximize the absolute values of cross-correlations (Sect. 2.7). Stippled areas are regions where time lags are not robustly specified, i.e., where the time lag envelope for $\Delta r = 0.05$ deviation from the maximum absolute correlation is greater than four months. See also Fig. S8 for the time lag patterns for different ENSO indices. (**b**) Maximum lagged cross-correlations between net carbon uptake anomaly and the ONI. (**c**) Lagged mean differences between net carbon uptake anomalies associated with El Niño and La Niña phases, with the same time lags as in (**a**). Stippling in (**b**) and (**c**) indicates areas where the correlation or the difference (based on a two-sided Welch's t-test) is not statistically significant at $p < 0.05$ level. (**d**) Regions sensitive to ENSO influences, identified from a clustering analysis based on the consistency of time lags among the ONI, Niño 3.4 Index, Multivariate ENSO Index, and Southern Oscillation Index and the statistical significance of corresponding lagged correlations (Sect. 2.7). Red dashed lines encompass grid cells of which the mean footprint sensitivity during 2007–2015 (Fig. S1) is among the top 80 % over North America. Grid cells with footprint sensitivity that falls in the bottom 20 % are excluded from the ENSO-sensitive regions for robustness. Also shown are median positions of the Pacific jet stream at 200 hPa in El Niño (dark red line with arrows) and La Niña winters (dark blue line with arrows), i.e., December–February, during 2007–2015.

https://doi.org/10.5194/egusphere-2026-880
Preprint. Discussion started: 13 April 2026

Although the majority of North America (Fig. S14) shows a positive lagged correlation between NBP anomalies and the ONI, that is, positive NBP anomalies (enhanced net carbon uptake) associated with El Niño, regional responses differ substantially (Fig. 1b). Notably, the Pacific coast, the southern Great Plains, and the Gulf Coast show the strongest positive correlations (Fig. 1b), and these correlations are statistically significant ($p < 0.05$). In contrast, northern Rocky Mountains, the Midwest, and Arctic tundra show negative and statistically significant correlations between NBP anomalies and the ONI (Fig. 1b), that is, negative NBP anomalies (reduced net carbon uptake) associated with El Niño. Most of the mid-continental regions do not show statistically significant correlations between NBP anomalies and the ONI, except part of the upper Midwest near the Great Lakes (Fig. 1b). These correlation patterns are broadly consistent across different ENSO indices (Fig. S9).

While the influence of ENSO on North American biome carbon uptake is widespread (Fig. 1b), the magnitude of these influences, defined by the mean difference in NBP anomaly between El Niño and La Niña-influenced periods (Sect. 2.8), is stronger in temperate than in boreal regions (Fig. 1c), consistent with previous studies (Hu et al., 2019; Liu et al., 2024). Furthermore, we find that ENSO's influences on net carbon uptake (El Niño minus La Niña; Fig. 1c) are stronger in regions where El Niño is associated with enhanced NBP (positive correlations in Fig. 1b) than in regions showing the opposite response (negative correlations in Fig. 1b; see also Fig. S15). When aggregated over North America, these contrasting regional responses give rise to the overall increase (decrease) of the North American terrestrial carbon sink associated with El Niño (La Niña) (Fig. 2); this response is robust to the posterior uncertainty of the inversion (Fig. S17). Although other Northern Hemisphere climate oscillations including the PNA pattern and the NAO may interact with ENSO in regulating phenology (Dannenberg et al., 2018) or regional carbon uptake (Parazoo et al., 2015), their influences on continental-scale carbon balance are not as prominent as ENSO (Fig. S7 and Table S11).

Interestingly, we identify distinct spatially-contiguous ENSO-sensitive regions (Fig. 1d) with consistent time lags (Fig. S8) and directions of response (Fig. S9) across multiple ENSO indices (Sect. 2.7). Note that these regions emerge directly from ENSO response patterns without being preconditioned upon specific biome or land use types (see Fig. S18 for biome fractions within each identified ENSO-sensitive region). In the following analyses, we focus on ENSO-sensitive regions in temperate North America, where space-time patterns of NBP are better constrained by available atmospheric CO_2 observations (Fig. S1). Within temperate North America, we identify three distinct regions where El Niño promotes net carbon uptake, namely the Pacific–Mountainous West (most of Oregon, southwestern Idaho, and northern California and Nevada), southern Great Plains, and central Gulf Coast (including part of the lower Mississippi River basin), spread across the prevalent path of the subtropical jet stream (Fig. 1d). These regions also overlap with some known hotspots of ENSO-driven hydroclimate impacts over North America (Trenberth et al., 1998; L'Heureux et al., 2015). We also identify three regions where El Niño is associated with reduced net carbon uptake, namely parts of the upper Midwest, the northern Rockies (including a western portion of the Canadian Prairies), and southern Appalachia (Fig. 1d). The latter group of ENSO-sensitive regions are less spatially contiguous than the regions showing enhanced uptake during El Niño.

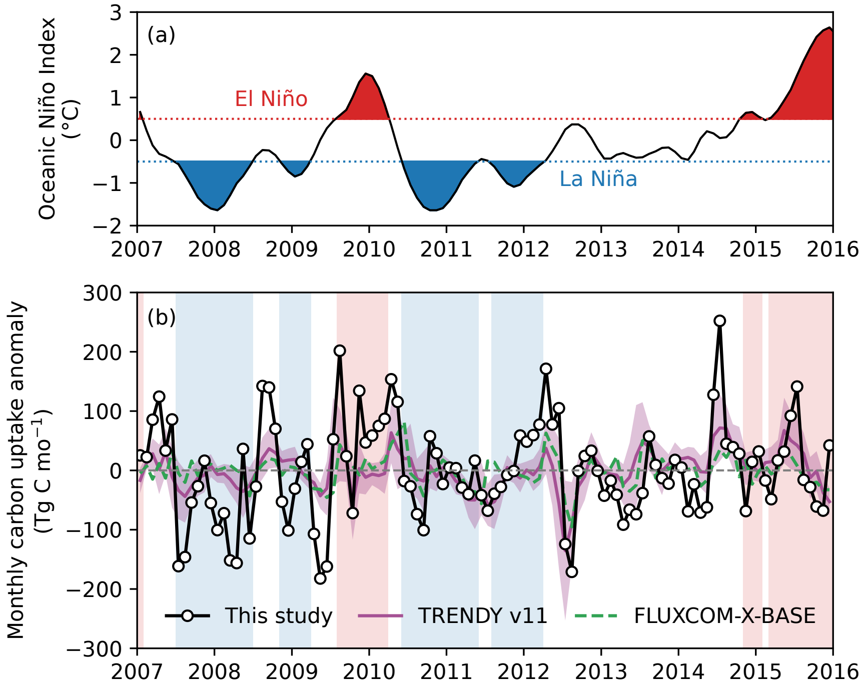

Figure 2. Terrestrial biosphere models and upscaled flux data do not capture ENSO-driven anomalies in the North American biospheric carbon sink during 2007–2015. (**a**) Monthly Oceanic Niño Index (ONI), with El Niño events labeled in red and La Niña events in blue. Thresholds for El Niño (0.5 °C) and La Niña (−0.5 °C) are denoted in dotted red and blue lines, respectively. (**b**) Monthly anomalies in net biome carbon uptake over North America from geostatistical inverse estimates in this study (empty circles and black line), from the mean of 16 terrestrial biosphere models (TBMs) in the TRENDY v11 ensemble (Friedlingstein et al., 2022) (purple), with light purple shading indicating ±1 standard deviation across TBMs (see Table S7 for the list of TBMs), and from the FLUXCOM-X-BASE machine learning model (Nelson et al., 2024) (green dashed line). A positive (negative) anomaly indicates enhanced (suppressed) net carbon uptake by the biosphere. El Niño and La Niña periods are marked by light red and light blue shadings, respectively. Monthly net carbon uptake anomalies based on geostatistical inverse estimates are positively and significantly correlated with the ONI ($r = 0.21$ and $p = 0.03$), whereas net carbon uptake anomalies from the TRENDY v11 ensemble mean ($r = 0.08$ and $p = 0.42$) or FLUXCOM-X-BASE ($r = 0.06$ and $p = 0.57$) do not show a significant correlation with the ONI. See also Fig. S16 for a similar comparison with NBP anomalies from individual members in the TRENDY v11 model ensemble, including the most and least responsive members (in terms of the absolute value of ENSO composite anomalies in NBP).

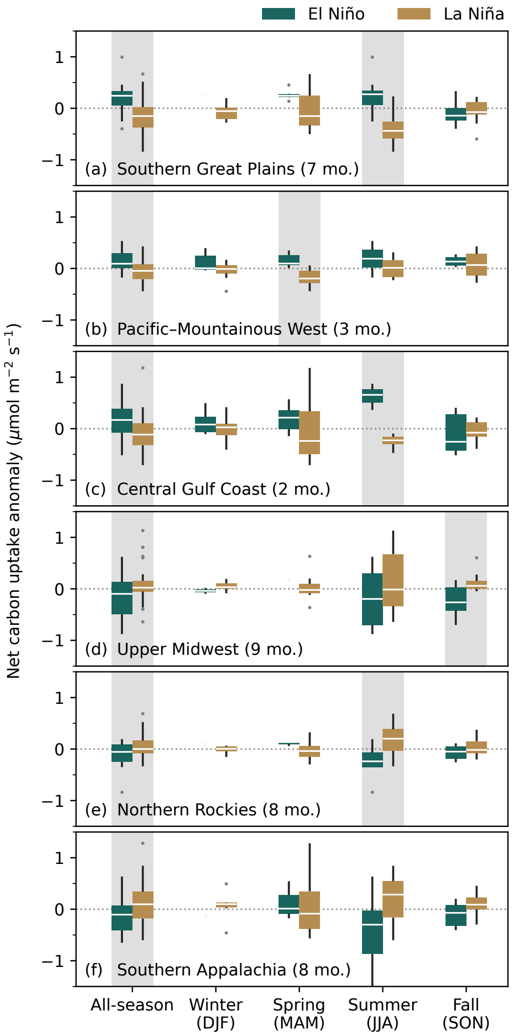

Figure 3. Seasonal patterns of ENSO impacts on net carbon uptake averaged over each ENSO-sensitive region. Definition of these regions follows Fig. 1d, and time lags are determined by maximizing the correlation between regionally-averaged net carbon uptake (i.e., NBP) anomalies and the Oceanic Niño Index. Monthly NBP anomalies influenced by El Niño (teal) and La Niña (brown) are compared within different climatological seasons and across all seasons, with time lags considered. Each box summarizes NBP anomalies associated with a specific ENSO phase within a season (or across all seasons), with the center bar, bounds of box, whiskers, and dots representing the median, first and third quartiles, smallest and largest anomalies falling within 1.5× of the interquartile range from the nearest quartiles, and outliers beyond that range, respectively. Pairs of El Niño and La Niña NBP anomalies that show statistically significant differences in a two-sided, two-sample Welch's t-test at $p < 0.05$ level are highlighted with light gray shading. Regions are ranked by the effect size (Cohen's d) for the difference between El Niño and La Niña NBP anomalies across all seasons (leftmost column): southern Great Plains ($d = 1.09$), Pacific–Mountainous West ($d = 0.98$), central Gulf Coast ($d = 0.68$), upper Midwest ($d = -0.68$), northern Rockies ($d = -0.70$), and southern Appalachia ($d = -0.72$).

3.2 Seasonal impact of ENSO phases on aggregated regional net carbon uptake anomalies

To further examine ENSO impacts on net carbon uptake in ENSO-sensitive regions (Fig. 1d), we identify time lags between regionally-aggregated NBP anomalies and ONI by maximizing the absolute value of their correlation, similar to those at the grid cell level (Sect. 2.7; see also Fig. S19). The resulting regional-level time lags are similar to those determined at the grid cell level (Figs. 1a and 3). All temperate regions sensitive to ENSO influences (labeled in Fig. 1d) show statistically significant differences ($p < 0.05$ in a two-sided, two-sample t-test) in aggregated NBP anomalies between El Niño and La Niña when considering all seasons (Fig. 3). Among them, the southern Great Plains and the Pacific–Mountainous West show stronger relative ENSO impact than other regions as measured by effect sizes (Fig. 3). The direction and magnitude of the ENSO impact on each region are robust given the uncertainty associated with the inversion-derived NBP estimates (Fig. S20). Interestingly, although the ENSO-sensitive regions are identified based on significant and consistent ENSO responses without relying on biome information, the fact that regions with strongest positive NBP responses to ENSO (southern Great Plains and Pacific–Mountainous West) are dominated by semi-arid biomes (grasslands, shrublands, and savannas; Fig. S18) suggests a potential role of water availability in modulating ENSO responses.

While El Niño and La Niña peak in winter (Fig. 2a), their impacts on net carbon uptake are concentrated in different seasons for different regions (Fig. 3; see also Fig. S21 for spatially explicit seasonal anomalies over North America). For regions that show enhanced NBP during El Niño, the enhancement is strongest in spring in the Pacific–Mountainous West (Fig. 3b) and summer in the southern Great Plains (Fig. 3a) and the central Gulf Coast (Fig. 3c), due primarily to different timing of the peak growing season (Fig. S13). For regions that show reduced NBP during El Niño, the reduction is highest in summer for northern Rockies (Fig. 3e) and fall for the upper Midwest (Fig. 3d), while not statistically significant at the seasonal timescale for southern Appalachia (Fig. 3f).

Taken together, these heterogeneous seasonal patterns of the responses of NBP anomalies to ENSO phases reflect the diverse teleconnection mechanisms through which ENSO exerts its impact on North American climate and net carbon uptake, reinforcing the need for a regional understanding of these impacts.

3.3 ENSO impacts on net carbon uptake anomalies mediated by energy and water availability

We find that a given response of net carbon uptake to ENSO can result from different local anomalies in energy availability (represented by temperature and shortwave radiation) or water availability (represented by precipitation, soil moisture, and vapor pressure deficit, VPD) across the identified ENSO-sensitive regions (Fig. 4), after controlling for the temporal autocorrelation in NBP (Sect. 2.9). Notably, the Pacific–Mountainous West is the only ENSO-sensitive region where the NBP anomaly is mainly controlled by energy availability rather than water availability (Fig. 4a). In other temperate ENSO-sensitive regions, NBP anomalies are regulated by different aspects of water availability across regions: precipitation, soil water stress, and atmospheric water demand. Below, we use standardized coefficients (Sect. 2.9; Table S8) to assess how local climate anomalies drive NBP anomalies in each ENSO-sensitive region.

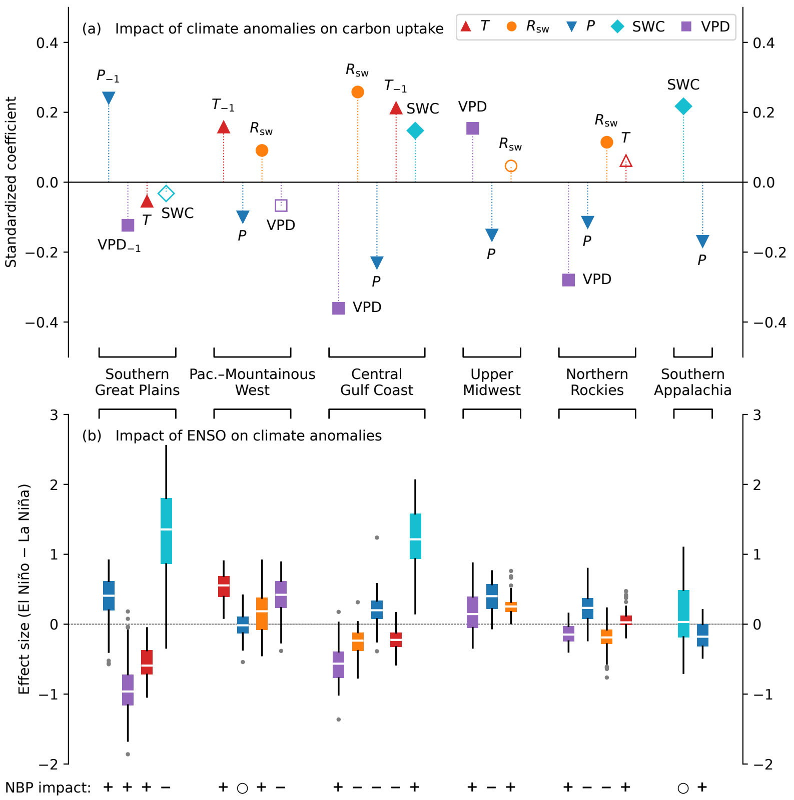

Figure 4. Attribution of net carbon uptake anomalies to climate anomalies across ENSO-sensitive regions. (**a**) Relative importance of climate anomalies in explaining net carbon uptake (i.e., NBP) anomalies at the grid cell level for each ENSO-sensitive region, from the most to the least important, as indicated by the absolute values of standardized coefficients. A positive (negative) standardized coefficient means an increase in the corresponding climate variable is associated with enhanced (suppressed) net carbon uptake. For each region, we identify climate anomalies in the preceding three months (labeled with numeric subscripts, for example, −1 for the anomaly in the previous month) that are most influential in explaining anomalies in net carbon uptake using statistical model selection (Sect. 2.9). Coefficients for NBP anomalies in the preceding month are omitted for clarity (Table S8). Empty symbols indicate variables that do not exert a robust influence on NBP anomalies, as their coefficients may flip sign in submodels (Sect. 2.9). Climate anomalies tested are: T, surface air temperature; P, precipitation rate; R_{sw}, incoming shortwave radiation; VPD, vapor pressure deficit; SWC, soil water content, from the North American Regional Reanalysis (Mesinger et al., 2006). (**b**) Direction and relative magnitude of ENSO influences on the anomalies in the same climate variables for each region as in (**a**), shown in effect sizes (Cohen's d). A positive (negative) effect size means that El Niño increases (decreases) the corresponding climate variable relative to La Niña. Effect sizes are calculated at the grid cell level (see Fig. 5b–f for maps) and binned as boxplots for visual assessment, with the center bar, bounds of box, whiskers, and dots representing the median, first and third quartiles, lowest and highest values falling within 1.5× of the interquartile range from the nearest quartiles, and outliers beyond that range, respectively. The NBP impact of each climate variable is indicated at the bottom of panel (**b**): a plus (minus) sign means that ENSO-induced anomalies tend to increase (decrease) NBP, whereas a circle indicates a non-significant influence (i.e., the effect size is not significantly different from zero based on a Z-test).

https://doi.org/10.5194/egusphere-2026-880
Preprint. Discussion started: 13 April 2026

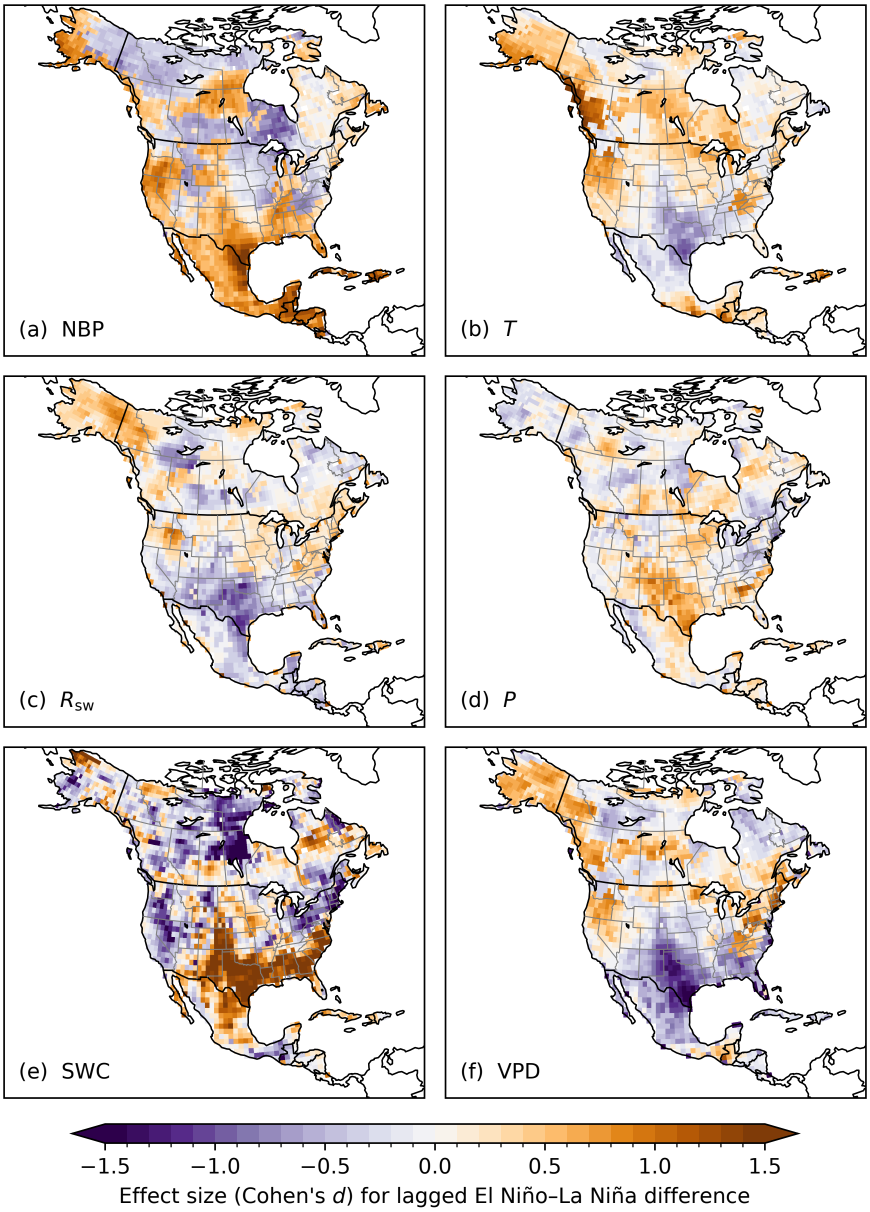

Figure 5. Effect sizes (Cohen's d) for differences in net carbon uptake anomalies and climate anomalies between ENSO phases. Effect 405 sizes are calculated from anomalies in net carbon uptake (NBP, **a**), air temperature (T, **b**), incoming shortwave radiation (R_{sw}, **c**), precipitation (P, **d**), soil water content (SWC, **e**), and vapor pressure deficit (VPD, **f**), grouped by El Niño- and La Niña-influenced months, with the same time lags for net carbon uptake anomalies shown in Fig. 1a considered. See also Fig. S22 for effect sizes for concurrent differences (i.e., without time lags).

https://doi.org/10.5194/egusphere-2026-880
Preprint. Discussion started: 13 April 2026

In the Pacific–Mountainous West, increased air temperatures (ΔT_{-1}, in the preceding month, Fig. 4b) and solar radiation (ΔR_{sw}, Fig. 4b) lead to enhanced net carbon uptake (positive ΔNBP, Fig. 3b) during El Niño. Given that ENSO's impact on the net carbon uptake of this region is most pronounced in spring (Fig. 3b), which is the peak growing season there (Fig. S13), it is likely that the warmer and sunnier conditions associated with El Niño (Fig. 5b and c) have enhanced peak carbon uptake when seasonal water stress has not yet begun. Although the warmer conditions during El Niño also lead to higher VPD (Figs. 4b and 5f), the influence of the VPD anomaly on the NBP anomaly is not robust in this region, as evidenced by the fact that its sign can flip depending on the presence or absence of other covariates (Table S9). In addition, because changes in precipitation associated with ENSO are not substantial in the Pacific–Mountainous West (Figs. 4b and 5d), El Niño does not appear to impose water limitation on net carbon uptake.

In contrast to the west coast, NBP anomalies in the southern Great Plains are more strongly regulated by water availability than energy availability (Fig. 4a), showing a dominant role of increased precipitation one month before (ΔP_{-1}) in enhancing NBP during El Niño (Fig. 4b). This mechanism is supported by the strong positive correlation between precipitation anomalies and the ONI in this region (Fig. S12h). In addition, reduced VPD and air temperature during El Niño (Fig. 4b), combined with the increased precipitation, further boost net carbon uptake in the southern Great Plains (Fig. 4a). This confluence of favorable conditions for NBP likely explains why this region shows the highest effect size of ENSO influence on NBP (Fig. 3a). Although El Niño also causes a strong increase in soil moisture over the southern Great Plains (Figs. 4b and 5e), the effect of the soil moisture anomaly on the NBP anomaly is not robust, as evidenced by the fact that its sign depends on the presence or absence of other covariates (Table S9).

While the Gulf Coast typically experiences similar ENSO climate impacts as the southern Great Plains, NBP anomalies in the central Gulf Coast region are predominantly regulated by VPD (Fig. 4a), with a substantial decrease during El Niño leading to enhanced NBP (Figs. 4b and 5f). The impacts of anomalies in shortwave radiation, temperature, precipitation, and soil moisture suggest a more nuanced picture of compensating influences. Increased soil moisture during El Niño (Figs. 4b and 5e) contributes to enhanced NBP (Fig. 4a), which is offset by the negative influences of reduced temperature and solar radiation (Fig. 4b) on NBP. Interestingly, increased precipitation during El Niño (Fig. 4b) suppresses NBP (Fig. 4a) in the central Gulf Coast region, possibly as a result of its correlation with reduced radiation. Overall, NBP anomalies in the central Gulf Coast show competing effects between water availability and energy availability, but reduced atmospheric water demand overwhelms other factors to boost NBP during El Niño.

In the upper Midwest, surprisingly, increased VPD during El Niño (Fig. 4b) leads to enhanced NBP (Fig. 4a), contrary to the overall response of reduced NBP during El Niño (Fig. 3d). This seemingly paradoxical effect of VPD on NBP results from a combination of different seasonal effects (Fig. S23). Whereas in winter and spring higher VPD is associated with enhanced NBP (Table S10), probably due to its co-occurrence with warmer conditions, in summer and fall higher VPD leads to reduced NBP (Table S10). Moreover, summer and fall NBP anomalies over the upper Midwest are most sensitive to precipitation anomalies (Fig. S23 and Table S10), indicating that excess late-season precipitation during El Niño (Fig. S24l) is more influential than VPD anomalies in suppressing net carbon uptake. Note that although the Midwest suffered from an exceptional drought in 2012 (Wolf et al., 2016), removing the year 2012 from our analysis does not result

https://doi.org/10.5194/egusphere-2026-880
Preprint. Discussion started: 13 April 2026

in substantial changes in the identified effects of precipitation and VPD on NBP anomalies in this region (Table S10). Thus, apart from the complication from season-dependent effects of VPD, it is mainly the heavier rainfall during El Niño that suppresses late-season NBP in the upper Midwest.

In the northern Rockies, El Niño leads to reduced VPD, increased precipitation, and reduced solar radiation (Figs. 4b and 5). Although the reduced VPD acts to enhance NBP (Fig. 4a), this effect is counteracted by increased precipitation and reduced solar radiation, both of which reduce NBP (Fig. 4a). The influence of temperature on NBP anomalies is not robust as its coefficient switches sign depending on other covariates (Table S9). Thus, it is the combined effect of excess precipitation and reduced solar radiation that suppresses NBP in the northern Rockies during El Niño, overwhelming the effect of reduced VPD. Note that the northern Rockies region identified here (northern Idaho, northwestern Montana, and southwestern Alberta) has a humid climate, unlike most of the arid western North America.

In southern Appalachia, reduced precipitation during El Niño (Fig. 4b) appears to lead to increased NBP (Fig. 4a), contrary to the overall response to El Niño (Fig. 3f), because this effect is also complicated by different seasonal effects (Fig. S23). Reduced precipitation leads to increased NBP in winter and spring, but reduced NBP in summer and fall (Fig. S23a and Table S10), consistent with seasonal impacts of ENSO on regionally-aggregated NBP in southern Appalachia (Fig. 3f; though these seasonal impacts are not statistically significant). Although the soil moisture anomaly contributes to the NBP anomaly (Fig. 4b), its role appears to be important only in winter and spring (Fig. S23a), with increased soil moisture enhancing NBP. When focusing on summer and fall NBP anomalies, warmer temperatures associated with El Niño are actually the most influential drivers of reduced NBP in southern Appalachia (Figs. S23 and S24d; see also Fig. 5b).

4 Discussion: Regional mechanisms key to ENSO impacts on the carbon cycle

While El Niño has been known to boost the North American terrestrial carbon sink (Hu et al., 2019), our findings reveal diverse and contrasting regional responses to ENSO that combine to yield this integrated continental response (Fig. 2).

Contrary to the previously reported east–west divide in the response of the North American carbon cycle to internal climate variability that had been based on coarse resolution top-down flux estimates (Byrne et al., 2020), and that followed the terrestrial aridity gradient (Seager et al., 2018), our analysis, enabled by a fine-scale regional inversion, reveals more nuanced ENSO impacts on net carbon uptake. In particular, the contrasting NBP responses to ENSO between Pacific and subtropical regions and mid-continental regions (Fig. 1c) reflect an indirect control by the position and intensity of the subtropical jet (Trenberth et al., 1998), mediated by the jet's impacts on North American temperature and hydroclimate anomalies (Seager et al., 2005; Deser et al., 2018; Jong et al., 2021). In other words, ENSO-driven changes in large-scale atmospheric circulation prevail over the terrestrial aridity gradient in determining the direction and magnitude of regional-scale responses of North American biome carbon uptake to ENSO.

How ENSO impacts on regional net carbon uptake are mediated by local climate anomalies is, however, preconditioned on the terrestrial aridity gradient. Among the identified temperate ENSO-sensitive regions (Figs. 1d and 4), NBP in semi-arid regions such as the southern Great Plains benefits from increased precipitation brought by El Niño, whereas in more humid regions, the impact of precipitation changes on NBP is secondary to that of temperature (Pacific–Mountainous West) or VPD (central Gulf Coast). Excess precipitation can even suppress late-season NBP during El Niño (upper Midwest and northern Rockies). Against the backdrop of large-scale circulation changes and terrestrial aridity gradients, each ENSO-sensitive region also shows specific local climate impacts from ENSO teleconnections as well as ecosystem responses.

The finding that NBP anomalies in the Pacific–Mountainous West (here, northern California and Nevada, Oregon, and southwestern Idaho; Fig. 1d) are primarily regulated by temperature and shortwave radiation rather than water availability (Fig. 4) appears at odds with the well-known El Niño impact of increased precipitation in California and reduced precipitation in Oregon and Washington (Jong et al., 2016; Deser et al., 2018). However, ENSO impacts on west coast precipitation can be unpredictable, with strong El Niño (La Niña) usually associated with increased (decreased) precipitation over California but moderate and weak El Niño (La Niña) associated with highly variable changes in precipitation (Hoell et al., 2016; Lee et al., 2018). For example, the 2011 La Niña was associated with anomalously high precipitation over the west coast due to strong atmospheric river activity, contrary to the expected response during La Niña (Luna-Niño et al., 2025), while the 2015/2016 exceptional El Niño failed to bring any increase in precipitation over California (Chen et al., 2021). Here, we find no statistically significant correlations between precipitation anomalies and the ONI on the Pacific coast during the study period (2007–2015), whereas temperature anomalies show robust positive correlations with the ONI (Figs. S12f and S25b). In addition, forests in the coastal Pacific Northwest are less limited by water than those in the interior Mountainous West (Seager et al., 2018; Zomer et al., 2022). These patterns of ENSO-driven climate variability—robust temperature anomalies but inconsistent precipitation anomalies—coupled with the ecohydrological context explain why temperature and shortwave radiation play more important roles in mediating NBP anomalies than hydrological variables in the identified Pacific–Mountainous West cluster.

Given the well-known hydroclimatic impacts on the southern Great Plains from ENSO (Kurtzman and Scanlon, 2007; Deser et al., 2018), it is unsurprising that both precipitation and VPD in the preceding month are important factors regulating NBP anomalies in this water-limited biome (Fig. 4a). However, the fact that summer is the season with the strongest ENSO impact on NBP (Fig. 3a) appears inconsistent with known ENSO impacts on winter precipitation. In recent years, the teleconnection between ENSO and Great Plains Low Level Jets (GPLLJs) has been increasingly recognized as an important mechanism in regulating summer precipitation in this region (Krishnamurthy et al., 2015; Liang et al., 2015). El Niño is typically associated with increased summer activity of GPLLJs (Krishnamurthy et al., 2015; Danco and Martin, 2018), which brings increased moisture supply from the Gulf of Mexico and facilitates deep convective activity and summer rainfall over the southern Great Plains (Stensrud, 1996). Here again, ENSO impacts on biome-scale net carbon uptake are mediated through interactions between ENSO and locally dominant weather systems.

Although El Niño has been known to bring more winter precipitation to the Gulf Coast (Kurtzman and Scanlon, 2007), its effect on summer precipitation is not significant in the region. Given that the growing season of this region does not start until April (as indicated by SIF), ENSO-driven anomalies in winter precipitation would have little immediate impact on the NBP (Fig. 3c). Instead, we find that VPD is the leading factor driving NBP anomalies in the central Gulf Coast (Fig. 4a), with reduced VPD during El Niño (Figs. 4b and 5f) leading to enhanced NBP. Even without increased summer precipitation (Fig. S24k), the year-round decrease in VPD during El Niño over this region (Hu et al., 2019) may have been sustained by local land–atmosphere feedbacks resulting from increased soil moisture (Chen and Kumar, 2002, 2004) (Fig. 5e). Although ENSO controls the annual water balance of the central Gulf Coast, its impact on NBP anomalies is likely mediated through the feedback from surface water storage to atmospheric evaporative demand.

There is a need to further characterize summer teleconnections in ENSO-sensitive regions in the continental interior (upper Midwest, northern Rockies, and southern Appalachia; Fig. 1d), given that ENSO impacts on summer climate have not been known to be prominent in these regions. Over the upper Midwest, the summer following peak El Niño when ENSO transitions to the La Niña phase is associated with anomalous anticyclonic patterns and warmer conditions (Jong et al., 2020), which may lead to reduced crop productivity (Anderson et al., 2017). Although we find positive temperature anomalies over the Midwest during El Niño (Fig. 5b and Fig. S24c and d), precipitation anomalies and their contribution to NBP anomalies vary by season (Fig. S23), highlighting a seasonal contrast in ENSO impacts on local climate and NBP anomalies in this region (Fig. 3d and Fig. S23). In the northern Rockies, century-long rain gauge data reveal a strong negative association between El Niño and winter precipitation (Stagge et al., 2023). As our study finds an eight-month lag of NBP anomalies in this region following El Niño (Figs. 1a and 3e), the similarly lagged ENSO impact on precipitation is highly variable across seasons (Fig. S24i–l) and sometimes contrary to its immediate impact on winter precipitation (Fig. S23b); the precipitation impact could also be complicated by topography in this region. While little is known about how ENSO impacts climate conditions in southern Appalachia, the attribution of late-season NBP anomalies suggests that warmer conditions lead to reduced NBP during El Niño (Fig. S23 and Table S10). Similarly, the attribution of NBP anomalies in southern Appalachia is complicated by varying topography and may require a more spatially-refined view to conclusively identify mechanisms of ENSO impacts. Targeted synoptic-scale studies (Randazzo et al., 2020) may help fill the gap in understanding ENSO's warm-season impacts on climate and carbon uptake in understudied mid-continental regions.

Taken together, the findings presented here point to a nuanced view of the regional-scale responses of terrestrial carbon fluxes to ENSO, elucidated by the high-resolution regional inverse model estimates of net biome carbon uptake over North America. The heterogeneous impacts of ENSO on biome-scale net carbon uptake (Figs. 1c and 3) are not a direct result of the typical "warmer northwest, wetter southeast" El Niño winter anomalies over North America, but rather involve spring warming that enhances carbon uptake during El Niño (e.g., the Pacific–Mountainous West) or land–atmosphere interactions such as increased soil moisture storage from winter precipitation sustaining a cooler-than-usual summer during El Niño (e.g., the central Gulf Coast). Fine-scale regional carbon flux estimates covering more ENSO cycles will be needed to illuminate the complex interplay among ENSO teleconnections, mesoscale climate, and the terrestrial carbon cycle, especially in light of the diversity of ENSO events (Capotondi et al., 2015) and projected future changes in ENSO (Cai et al., 2021).

A better understanding of region-specific mechanisms underlying ENSO-driven net carbon uptake anomalies may also translate into improved representation of the sensitivity of carbon fluxes to energy and water availability in terrestrial biosphere models, and more broadly, better constrained carbon–climate feedbacks. Although terrestrial biosphere models represent these sensitivities as general physiological responses that are not specific to ENSO, the fact that they underestimate ENSO-driven flux anomalies (Fig. 2) indicates a widespread misrepresentation of the sensitivity of carbon fluxes to temperature and hydroclimate anomalies for North American biomes (Shiga et al., 2018a; Hu et al., 2019). This misrepresentation impacts the assessment of carbon–climate feedbacks, as uncertainty in the sensitivity of carbon fluxes to climate anomalies propagates into future carbon cycle projections. Moreover, as models may show seemingly correct responses for the wrong reasons when tuned to insufficient observational constraints, a pervasive issue known as error compensation (Balaji et al., 2022), ENSO as the leading mode of internal climate variability offers an opportunity to explore terrestrial biosphere models' misrepresentation of the sensitivity of carbon fluxes to climate anomalies and facilitate model improvements for robust long-term carbon cycle and climate projections.

Taking a global view, our findings highlight a robust partial compensation between carbon flux anomalies over tropical and extratropical lands driven by known ENSO teleconnections over the Pacific–North American sector. This compensation has hitherto been overlooked in understanding of the global carbon cycle's sensitivity to internal climate variability. Anomalies in the global atmospheric CO_2 growth rate have been attributed primarily to ENSO-driven temperature anomalies over the tropics (Cox et al., 2013) and this relationship has been used to constrain the tropical carbon–climate feedback from earth system model projections. This simplistic view overlooks the responses of carbon fluxes in extratropical lands to ENSO, which often act in opposition to the responses of tropical lands, as revealed in recent studies (Hu et al., 2019; Liu et al., 2024). Notably, the 2021 La Niña, though not covered in our study period, led to reduced net carbon uptake in the northern extratropics, offsetting over 70 % of the estimated carbon uptake enhancement in the tropics (Liu et al., 2024) and challenging the long-standing interpretation of CO_2 growth rate anomalies as an indicator of tropical carbon–climate feedback (Cox et al., 2013; Wang et al., 2014; Luo and Keenan, 2022). Given that ENSO teleconnections are widespread over extratropical lands beyond North America (Trenberth et al., 1998), there may exist yet undiscovered links between ENSO and terrestrial carbon flux anomalies over other extratropical regions. It has also been noted that extreme El Niño events may break this compensation pattern, leading to increased carbon emissions from both tropical and extratropical lands and amplifying the carbon cycle's sensitivity to internal climate variability (Li et al., 2024). There is also a need to further understand how ENSO impacts on regional carbon cycling differ across ENSO events of varying strength and localization (e.g., central Pacific vs. eastern Pacific El Niño events) (Dannenberg and Johnston, 2023). As a warming climate is projected to bring more frequent extreme El Niño and La Niña events (Cai et al., 2014, 2015) and intensify the jet stream (Shaw and Miyawaki, 2023), characterizing the dynamic and physiological mechanisms as well as global-to-regional linkages controlling carbon cycle responses to ENSO, in both tropical and extratropical lands, will be increasingly important for attributing and predicting changes in the carbon cycle.

Appendix A: Implementation of geostatistical inverse modeling for CO_2 flux estimation

We use multivariate linear regression to select a parsimonious set of explanatory variables to capture observed variability in biospheric CO_2 drawdowns or enhancements (Gourdji et al., 2012; Miller et al., 2018; Shiga et al., 2018b). The variable

https://doi.org/10.5194/egusphere-2026-880
Preprint. Discussion started: 13 April 2026

selection helps to minimize the risk of biasing flux estimates due to spurious correlations. Following Shiga et al. (2018b), the regression is posed as:

$$\mathbf{z} = \mathbf{H}\mathbf{X}\boldsymbol{\beta} \quad \boldsymbol{\epsilon}, \tag{A1}$$

where $\mathbf{z}$ is a column vector of observed biospheric CO_2 drawdowns or enhancements (μmol mol^{-1}), $\mathbf{H}$ is a matrix that aggregates WRF–STILT transport footprints (m^2 s mol^{-1}), $\mathbf{X}$ represents covariates of CO_2 fluxes (vegetation indicators and climate drivers), $\boldsymbol{\beta}$ is a column vector of linear coefficients to link the atmospheric signals resulting from the explanatory variables with observed CO_2 variability, and $\boldsymbol{\epsilon}$ is the combined error term incorporating measurement error, transport error, model–data mismatch, and residuals not explained by the explanatory variables. We run the regression for all possible combinations of explanatory variables and identify the combination that optimally explains atmospheric CO_2 variability based on the Schwarz Bayesian information criterion (Schwarz, 1978), using a branch-and-bound algorithm (Yadav et al., 2013). The selection yields an optimal model that includes kriged GOME-2A solar-induced chlorophyll fluorescence (SIF) retrieval (mW m^{-2} nm^{-1} sr^{-1}), specific humidity (kg kg^{-1}), and precipitation rate (kg m^{-2} s^{-1}) as the covariates to explain variability in observed CO_2 concentrations.

The geostatistical inverse modeling (GIM) approach leverages a set of covariates (identified above) to explain a portion of the variability in CO_2 fluxes and a prior error covariance model to characterize the deviation of CO_2 fluxes from the deterministic trend explained by these covariates (Michalak et al., 2004; Gourdji et al., 2010). The GIM approach has the advantage of requiring no prior flux estimates and making no assumptions about the spatiotemporal flux covariance structure beyond a functional form and is thus more directly informed by data (Gourdji et al., 2012) than typical prior-based Bayesian inversions. Here, we pose the GIM approach as minimizing the following objective function:

$$L(\mathbf{s},\boldsymbol{\beta}) = \frac{1}{2}\left[(\mathbf{z}-\mathbf{H}\mathbf{s})^{\top}\mathbf{R}^{-1}(\mathbf{z}-\mathbf{H}\mathbf{s}) \quad (\mathbf{s}-\mathbf{X}\boldsymbol{\beta})^{\top}\mathbf{Q}^{-1}(\mathbf{s}-\mathbf{X}\boldsymbol{\beta})\right], \tag{A2}$$

where $\mathbf{s}$ represents the surface fluxes (μmol m^{-2} s^{-1}) to be estimated, discretized in space and time, $\mathbf{z}$ and $\mathbf{H}$ are the same as in Eq. (A1), $\mathbf{X}$ represents the explanatory variables identified from model selection, with additional columns to capture the diurnal cycles of fluxes (detailed below), $\boldsymbol{\beta}$ represents the linear coefficients for the explanatory variables, including for the columns that represent diurnal cycles, $\mathbf{R}$ is the model–data mismatch covariance matrix, here assumed to be diagonal, and $\mathbf{Q}$ is the prior flux covariance matrix, which contains off-diagonal elements.

Because sub-monthly and monthly explanatory variables like SIF and climate drivers do not capture the diurnal cycles of fluxes, we use additional columns to represent the fast-varying diurnal component of fluxes in each month relative to the slow-varying component captured by SIF and climate drivers. Given that the transport footprints were aggregated at three-hourly temporal resolution, eight columns indicating different hours are needed to resolve the mean diurnal cycle for each month. For 12 months in a year, 96 indicator columns are needed. These indicator columns are encoded following one-hot encoding. For example, to represent the diurnal component at 03:00 in January 2007, any rows in $\mathbf{X}$ that represent 03:00 and fall within January 2007 are filled with ones and the rest are filled with zeros. The linear coefficient in $\boldsymbol{\beta}$ that corresponds to this column is solved by optimizing the objective function L. This approach imposes little restriction on the diurnal cycle, but instead leverages as much information as is available in atmospheric CO_2 observations.

https://doi.org/10.5194/egusphere-2026-880
Preprint. Discussion started: 13 April 2026

We assume that model–data mismatch errors, including measurement, representation, and transport errors, are uncorrelated across 61 CO_2 monitoring sites and in time, which means that $\mathbf{R}$ is a diagonal matrix (Mueller et al., 2008; Gourdji et al., 2010). The diagonal elements, that is, model–data mismatch variances, $\sigma^2_{\mathrm{R}}(i,j)$, are optimized for each site (i) in each month (j).

The covariance matrix $\mathbf{Q}$, which characterizes the spatiotemporal autocorrelation in the stochastic component of the fluxes, is represented using an isotropic exponential decay covariance function (Michalak et al., 2004; Gourdji et al., 2010):

$$\mathbf{Q}\left(h_x, h_t \mid \sigma^2_{\mathrm{Q}}, \ell, \tau\right) = \sigma^2_{\mathrm{Q}} \exp\left(-\frac{h_x}{\ell}\right) \exp\left(-\frac{h_t}{\tau}\right), \tag{A3}$$

where h_x (km) and h_t (d) are the distances between grid cells in space and in time, respectively, ℓ (km) and τ (d) are the spatial and temporal correlation parameters, and σ^2_{Q} is the asymptotic variance of fluxes at large distances. The parameters σ^2_{Q}, ℓ, and τ, which define $\mathbf{Q}$, are optimized together with the variance parameters that define $\mathbf{R}$ for each month using restricted maximum likelihood optimization described in Gourdji et al. (2010). The optimized parameters for the study period are listed in Tables S4–S6.

With the covariance matrices $\mathbf{Q}$ and $\mathbf{R}$ specified, we solve for the posterior estimates of the fluxes, $\hat{\mathbf{s}}$, and the linear coefficients, $\hat{\boldsymbol{\beta}}$, from the geostatistical inverse linear system of equations (Michalak et al., 2004) using an efficient algorithm of $\mathcal{O}(n^{2.5})$ complexity described in Yadav and Michalak (2013). The objective function L is optimized each month, which means surface fluxes ($\hat{\mathbf{s}}$) are solved for each month at three-hourly temporal resolution. We then average the flux estimates monthly for analyses of flux anomalies. See Fig. S2 for the mean seasonal cycle of flux patterns.

Following Michalak et al. (2004), the posterior covariance of the flux estimates $\hat{\mathbf{s}}$ are given by

$$\mathbf{V}_{\hat{\mathbf{s}}} = -\mathbf{X}\mathbf{M} \quad \mathbf{Q} - \mathbf{Q}\mathbf{H}^\top \boldsymbol{\Lambda}^\top, \tag{A4}$$

where $\boldsymbol{\Lambda}$ and $\mathbf{M}$ are obtained from solving the linear system

$$\begin{bmatrix} \mathbf{H}\mathbf{Q}\mathbf{H}^\top \quad \mathbf{R} & \mathbf{H}\mathbf{X} \\ (\mathbf{H}\mathbf{X})^\top & \mathbf{0} \end{bmatrix} \begin{bmatrix} \boldsymbol{\Lambda}^\top \\ \mathbf{M} \end{bmatrix} = \begin{bmatrix} \mathbf{H}\mathbf{Q} \\ \mathbf{X}^\top \end{bmatrix}. \tag{A5}$$

The posterior flux uncertainty for each grid cell is then calculated as the square root of the diagonal elements of $\mathbf{V}_{\hat{\mathbf{s}}}$ (Michalak et al., 2004). See Fig. S3 for a summary of the uncertainty and relative uncertainty in monthly mean flux estimates by season and latitudinal band.

Code and data availability. Code used to generate figures and results presented in this study is available at https://gitlab.com/wusun/enso-impact-na-carbon-flux. SIF-driven geostatistical inverse estimates of North American land carbon fluxes will be released to Zenodo upon publication. The ObsPack GLOBALVIEWplus CO_2 data product is available at https://gml.noaa.gov/ccgg/obspack/. The CarbonTracker-Lagrange WRF–STILT footprints are available at https://gml.noaa.gov/ccgg/carbontracker-lagrange/. Access to the TRENDY v11 model ensemble can be requested at the data hub of the Global Carbon Budget (https://globalcarbonbudgetdata.org/closed-access-requests.html). The FLUXCOM-X-BASE data products are available through the Integrated Carbon Observation System (ICOS) data portal (https://doi.org/10.18160/5NZG-JMJE). The FFDAS v2 data product is available at https://ffdas.rc.nau.edu/. The North American Regional Reanalysis data can be obtained at https://psl.noaa.gov/data/gridded/data.narr.html.

Author contributions. W.S., K.T.F., Y.P.S., N.A.R., and A.M.M. designed research. W.S., K.T.F., Y.P.S., J.M., N.A.R., and A.M.M. performed research. W.S., Y.P.S., J.M., N.A.R., and A.M.M. contributed methods. W.S., Y.P.S., J.M., and N.A.R. analyzed data. W.S., K.T.F., and J.M. wrote the initial draft. W.S., K.T.F., J.M., N.A.R., and A.M.M. performed revision of the draft. All authors reviewed and approved the final draft.

Competing interests. The authors declare no competing interests.

Acknowledgements. We thank the National Oceanic and Atmospheric Administration (NOAA) Global Monitoring Laboratory and principal investigators of individual monitoring sites for providing atmospheric CO_2 observations. We thank the following individual for collecting and providing in situ atmospheric CO_2 observations over North America: Arlyn E. Andrews, Sébastien C. Biraud, Kenneth J. Davis, Marc L. Fischer, Timothy J. Griffis, Daniel A. Jaffe, Beverly E. Law, Kathryn McKain, Natasha L. Miles, John B. Miller, Matthew J. Parker, Scott J. Richardson, Britton B. Stephens, Colm Sweeney, Pieter P. Tans, Kirk Thoning, Margaret S. Torn, Stephan De Wekker, Steven C. Wofsy, and Douglas E. J. Worthy. WRF–STILT atmospheric transport simulations were supported by the NASA award "Regional Inverse Modeling in North and South America for the NASA Carbon Monitoring System." We thank Thomas Nehrkorn, John M. Henderson, and Janusz Eluszkiewicz at Atmospheric and Environmental Research, Inc. for conducting WRF–STILT simulations and the CarbonTracker-Lagrange team (https://www.esrl.noaa.gov/gmd/ccgg/carbontracker-lagrange/) for archiving and providing WRF–STILT transport footprints. We thank Kirk Thoning for providing CO_2 background concentration estimates based on free troposphere and marine boundary layer measurements.

We thank Stephen Sitch, Pierre Friedlingstein, and all modelers who have contributed to the "Trends and drivers of the regional scale terrestrial sources and sinks of carbon dioxide" (TRENDY) project version 11 (https://globalcarbonbudgetdata.org/index.html). We thank the FLUXCOM-X team for the FLUXCOM-X-BASE net ecosystem exchange data product. We acknowledge the National Centers for Environmental Prediction North American Regional Reanalysis data provided by the NOAA Physical Sciences Laboratory, Boulder, Colorado, USA, obtained from their website at https://psl.noaa.gov/. We thank NOAA Physical Sciences Laboratory (https://psl.noaa.gov/) and NOAA National Weather Service Climate Prediction Center (https://www.cpc.ncep.noaa.gov/) for providing ENSO indices. We thank Kevin Gurney for the FFDAS v2 data product. We thank Jovan Tadić for the kriged GOME-2A SIF data. We thank Guido van der Werf for the Global Fire Emissions Database version 4.1s (van der Werf et al., 2017; Randerson et al., 2018).

We thank Garret Huntress and Maria Lopez for assistance in computation. We thank Bridger Ruyle and Weiwei Zhan for feedback on data visualization. Computations presented in this study were conducted through the Carnegie Institution for Science's partnership in the Resnick High Performance Computing Center (https://www.hpc.caltech.edu), a facility supported by Resnick Sustainability Institute at the California Institute of Technology.

This study is a contribution to the North American Carbon Program (https://www.nacarbon.org).

Financial support. This study received support from the National Aeronautics and Space Administration (NASA) through the Carbon Monitoring System award #80NSSC18K0165. W.S. acknowledges support from the Carnegie Institution for Science's endowment fund.

References

Anderson, W., Seager, R., Baethgen, W., and Cane, M.: Life cycles of agriculturally relevant ENSO teleconnections in North and South America, International Journal of Climatology, 37, 3297–3318, https://doi.org/10.1002/joc.4916, 2017.

Asefi-Najafabady, S., Rayner, P. J., Gurney, K. R., McRobert, A., Song, Y., Coltin, K., Huang, J., Elvidge, C., and Baugh, K.: A multiyear, global gridded fossil fuel CO_2 emission data product: Evaluation and analysis of results, Journal of Geophysical Research: Atmospheres, 119, 10 213–10 231, https://doi.org/10.1002/2013JD021296, 2014.

Bacastow, R. B.: Modulation of atmospheric carbon dioxide by the Southern Oscillation, Nature, 261, 116–118, https://doi.org/10.1038/261116a0, 1976.

Balaji, V., Couvreux, F., Deshayes, J., Gautrais, J., Hourdin, F., and Rio, C.: Are general circulation models obsolete?, Proceedings of the National Academy of Sciences, 119, e2202075 119, https://doi.org/10.1073/pnas.2202075119, 2022.

Bastos, A., Running, S. W., Gouveia, C., and Trigo, R. M.: The global NPP dependence on ENSO: La Niña and the extraordinary year of 2011, Journal of Geophysical Research: Biogeosciences, 118, 1247–1255, https://doi.org/10.1002/jgrg.20100, 2013.

Bastos, A., Friedlingstein, P., Sitch, S., Chen, C., Mialon, A., Wigneron, J.-P., Arora, V. K., Briggs, P. R., Canadell, J. G., Ciais, P., Chevallier, F., Cheng, L., Delire, C., Haverd, V., Jain, A. K., Joos, F., Kato, E., Lienert, S., Lombardozzi, D., Melton, J. R., Myneni, R., Nabel, J. E. M. S., Pongratz, J., Poulter, B., Rödenbeck, C., Séférian, R., Tian, H., van Eck, C., Viovy, N., Vuichard, N., Walker, A. P., Wiltshire, A., Yang, J., Zaehle, S., Zeng, N., and Zhu, D.: Impact of the 2015/2016 El Niño on the terrestrial carbon cycle constrained by bottom-up and top-down approaches, Philosophical Transactions of the Royal Society B: Biological Sciences, 373, 20170 304, https://doi.org/10.1098/rstb.2017.0304, 2018.

Betts, R. A., Burton, C. A., Feely, R. A., Collins, M., Jones, C. D., and Wiltshire, A. J.: ENSO and the carbon cycle, chap. 20, pp. 453–470, American Geophysical Union, ISBN 9781119548164, https://doi.org/10.1002/9781119548164.ch20, 2020.

Bjerknes, J.: Atmospheric teleconnections from the equatorial Pacific, Monthly Weather Review, 97, 163–172, https://doi.org/10.1175/1520-0493(1969)097<0163:ATFTEP>2.3.CO;2, 1969.

Burton, C., Betts, R. A., Jones, C. D., Feldpausch, T. R., Cardoso, M., and Anderson, L. O.: El Niño Driven Changes in Global Fire 2015/16, Frontiers in Earth Science, 8, 199, https://doi.org/10.3389/feart.2020.00199, 2020.

Byrne, B., Liu, J., Bloom, A. A., Bowman, K. W., Butterfield, Z., Joiner, J., Keenan, T. F., Keppel-Aleks, G., Parazoo, N. C., and Yin, Y.: Contrasting regional carbon cycle responses to seasonal climate anomalies across the east-west divide of temperate North America, Global Biogeochemical Cycles, 34, e2020GB006 598, https://doi.org/10.1029/2020GB006598, 2020.

Byrne, B., Baker, D. F., Basu, S., Bertolacci, M., Bowman, K. W., Carroll, D., Chatterjee, A., Chevallier, F., Ciais, P., Cressie, N., Crisp, D., Crowell, S., Deng, F., Deng, Z., Deutscher, N. M., Dubey, M. K., Feng, S., García, O. E., Griffith, D. W. T., Herkommer, B., Hu, L., Jacobson, A. R., Janardanan, R., Jeong, S., Johnson, M. S., Jones, D. B. A., Kivi, R., Liu, J., Liu, Z., Maksyutov, S., Miller, J. B., Miller, S. M., Morino, I., Notholt, J., Oda, T., O'Dell, C. W., Oh, Y.-S., Ohyama, H., Patra, P. K., Peiro, H., Petri, C., Philip, S., Pollard, D. F., Poulter, B., Remaud, M., Schuh, A., Sha, M. K., Shiomi, K., Strong, K., Sweeney, C., Té, Y., Tian, H., Velazco, V. A., Vrekoussis, M., Warneke, T., Worden, J. R., Wunch, D., Yao, Y., Yun, J., Zammit-Mangion, A., and Zeng, N.: National CO_2 budgets (2015–2020) inferred from atmospheric CO_2 observations in support of the global stocktake, Earth System Science Data, 15, 963–1004, https://doi.org/10.5194/essd-15-963-2023, 2023.

Byrne, B., Liu, J., Bowman, K. W., Pascolini-Campbell, M., Chatterjee, A., Pandey, S., Miyazaki, K., van der Werf, G. R., Wunch, D., Wennberg, P. O., Roehl, C. M., and Sinha, S.: Carbon emissions from the 2023 Canadian wildfires, Nature, 633, 835–839, https://doi.org/10.1038/s41586-024-07878-z, 2024.

Cai, W., Borlace, S., Lengaigne, M., van Rensch, P., Collins, M., Vecchi, G., Timmermann, A., Santoso, A., McPhaden, M. J., Wu, L., England, M. H., Wang, G., Guilyardi, E., and Jin, F.-F.: Increasing frequency of extreme El Niño events due to greenhouse warming, Nature Climate Change, 4, 111–116, https://doi.org/10.1038/nclimate2100, 2014.

Cai, W., Wang, G., Santoso, A., McPhaden, M. J., Wu, L., Jin, F.-F., Timmermann, A., Collins, M., Vecchi, G., Lengaigne, M., England, M. H., Dommenget, D., Takahashi, K., and Guilyardi, E.: Increased frequency of extreme La Niña events under greenhouse warming, Nature Climate Change, 5, 132–137, https://doi.org/10.1038/nclimate2492, 2015.

Cai, W., Santoso, A., Collins, M., Dewitte, B., Karamperidou, C., Kug, J.-S., Lengaigne, M., McPhaden, M. J., Stuecker, M. F., Taschetto, A. S., Timmermann, A., Wu, L., Yeh, S.-W., Wang, G., Ng, B., Jia, F., Yang, Y., Ying, J., Zheng, X.-T., Bayr, T., Brown, J. R., Capotondi, A., Cobb, K. M., Gan, B., Geng, T., Ham, Y.-G., Jin, F.-F., Jo, H.-S., Li, X., Lin, X., McGregor, S., Park, J.-H., Stein, K., Yang, K., Zhang, L., and Zhong, W.: Changing El Niño–Southern Oscillation in a warming climate, Nature Reviews Earth & Environment, 2, 628–644, https://doi.org/10.1038/s43017-021-00199-z, 2021.

Capotondi, A., Wittenberg, A. T., Newman, M., Lorenzo, E. D., Yu, J.-Y., Braconnot, P., Cole, J., Dewitte, B., Giese, B., Guilyardi, E., Jin, F.-F., Karnauskas, K., Kirtman, B., Lee, T., Schneider, N., Xue, Y., and Yeh, S.-W.: Understanding ENSO diversity, Bulletin of the American Meteorological Society, 96, 921–938, https://doi.org/10.1175/bams-d-13-00117.1, 2015.

Chapin, F. S., Woodwell, G. M., Randerson, J. T., Rastetter, E. B., Lovett, G. M., Baldocchi, D. D., Clark, D. A., Harmon, M. E., Schimel, D. S., Valentini, R., Wirth, C., Aber, J. D., Cole, J. J., Goulden, M. L., Harden, J. W., Heimann, M., Howarth, R. W., Matson, P. A., McGuire, A. D., Melillo, J. M., Mooney, H. A., Neff, J. C., Houghton, R. A., Pace, M. L., Ryan, M. G., Running, S. W., Sala, O. E., Schlesinger, W. H., and Schulze, E.-D.: Reconciling carbon-cycle concepts, terminology, and methods, Ecosystems, 9, 1041–1050, https://doi.org/10.1007/s10021-005-0105-7, 2006.

Chen, D., Norris, J., Goldenson, N., Thackeray, C., and Hall, A.: A distinct atmospheric mode for California precipitation, Journal of Geophysical Research: Atmospheres, 126, e2020JD034 403, https://doi.org/10.1029/2020JD034403, 2021.

Chen, J. and Kumar, P.: Role of terrestrial hydrologic memory in modulating ENSO impacts in North America, Journal of Climate, 15, 3569–3585, https://doi.org/10.1175/1520-0442(2003)015<3569:ROTHMI>2.0.CO;2, 2002.

Chen, J. and Kumar, P.: A modeling study of the ENSO influence on the terrestrial energy profile in North America, Journal of Climate, 17, 1657–1670, https://doi.org/10.1175/1520-0442(2004)017<1657:AMSOTE>2.0.CO;2, 2004.

Chen, S., Stark, S. C., Nobre, A. D., Cuartas, L. A., de Jesus Amore, D., Restrepo-Coupe, N., Smith, M. N., Chitra-Tarak, R., Ko, H., Nelson, B. W., and Saleska, S. R.: Amazon forest biogeography predicts resilience and vulnerability to drought, Nature, 631, 111–117, https://doi.org/10.1038/s41586-024-07568-w, 2024.

Chen, Y., Morton, D. C., Andela, N., van der Werf, G. R., Giglio, L., and Randerson, J. T.: A pan-tropical cascade of fire driven by El Niño/Southern Oscillation, Nature Climate Change, 7, 906–911, https://doi.org/10.1038/s41558-017-0014-8, 2017.

Cooperative Global Atmospheric Data Integration Project: Multi-laboratory compilation of atmospheric carbon dioxide data for the period 1957–2016; obspack_co2_1_GLOBALVIEWplus_v3.2_2017-11-02, https://doi.org/10.15138/g3704h, 2017.

Cox, P. M., Pearson, D., Booth, B. B., Friedlingstein, P., Huntingford, C., Jones, C. D., and Luke, C. M.: Sensitivity of tropical carbon to climate change constrained by carbon dioxide variability, Nature, 494, 341–344, https://doi.org/10.1038/nature11882, 2013.

Danco, J. F. and Martin, E. R.: Understanding the influence of ENSO on the Great Plains low-level jet in CMIP5 models, Climate Dynamics, 51, 1537–1558, https://doi.org/10.1007/s00382-017-3970-9, 2018.

Dannenberg, M. P. and Johnston, M. R.: Effects of eastern vs. central Pacific El Niño on Northern Hemisphere photosynthetic seasonality, Environmental Research: Climate, 2, 031 002, https://doi.org/10.1088/2752-5295/accb02, 2023.

Dannenberg, M. P., Song, C., Hwang, T., and Wise, E. K.: Empirical evidence of El Niño–Southern Oscillation influence on land surface phenology and productivity in the western United States, Remote Sensing of Environment, 159, 167–180, https://doi.org/10.1016/j.rse.2014.11.026, 2015.

Dannenberg, M. P., Wise, E. K., Janko, M., Hwang, T., and Smith, W. K.: Atmospheric teleconnection influence on North American land surface phenology, Environmental Research Letters, 13, 034 029, https://doi.org/10.1088/1748-9326/aaa85a, 2018.

Dannenberg, M. P., Smith, W. K., Zhang, Y., Song, C., Huntzinger, D. N., and Moore, D. J. P.: Large-Scale Reductions in Terrestrial Carbon Uptake Following Central Pacific El Niño, Geophysical Research Letters, 48, e2020GL092 367, https://doi.org/10.1029/2020GL092367, 2021.

Deser, C., Simpson, I. R., Phillips, A. S., and McKinnon, K. A.: How well do we know ENSO's climate impacts over North America, and how do we evaluate models accordingly?, Journal of Climate, 31, 4991–5014, https://doi.org/10.1175/jcli-d-17-0783.1, 2018.

Du, J., Kimball, J. S., Sheffield, J., Velicogna, I., Zhao, M., Pan, M., Fisher, C. K., Beck, H. E., Watts, J. D., A, G., and Wood, E. F.: Synergistic satellite assessment of global vegetation health in relation to ENSO-induced droughts and pluvials, Journal of Geophysical Research: Biogeosciences, 126, e2020JG006 006, https://doi.org/10.1029/2020JG006006, 2021.

Fang, Y. and Michalak, A. M.: Atmospheric observations inform CO_2 flux responses to enviroclimatic drivers, Global Biogeochemical Cycles, 29, 555–566, https://doi.org/10.1002/2014GB005034, 2015.

Fang, Y., Michalak, A. M., Shiga, Y. P., and Yadav, V.: Using atmospheric observations to evaluate the spatiotemporal variability of CO_2 fluxes simulated by terrestrial biospheric models, Biogeosciences, 11, 6985–6997, https://doi.org/10.5194/bg-11-6985-2014, 2014.

Fang, Y., Michalak, A. M., Schwalm, C. R., Huntzinger, D. N., Berry, J. A., Ciais, P., Piao, S., Poulter, B., Fisher, J. B., Cook, R. B., Hayes, D., Huang, M., Ito, A., Jain, A., Lei, H., Lu, C., Mao, J., Parazoo, N. C., Peng, S., Ricciuto, D. M., Shi, X., Tao, B., Tian, H., Wang, W., Wei, Y., and Yang, J.: Global land carbon sink response to temperature and precipitation varies with ENSO phase, Environmental Research Letters, 12, 064 007, https://doi.org/10.1088/1748-9326/aa6e8e, 2017.

Frankenberg, C., Fisher, J. B., Worden, J., Badgley, G., Saatchi, S. S., Lee, J.-E., Toon, G. C., Butz, A., Jung, M., Kuze, A., and Yokota, T.: New global observations of the terrestrial carbon cycle from GOSAT: Patterns of plant fluorescence with gross primary productivity, Geophysical Research Letters, 38, L17 706, https://doi.org/10.1029/2011GL048738, 2011.

Friedlingstein, P., O'Sullivan, M., Jones, M. W., Andrew, R. M., Gregor, L., Hauck, J., Le Quéré, C., Luijkx, I. T., Olsen, A., Peters, G. P., Peters, W., Pongratz, J., Schwingshackl, C., Sitch, S., Canadell, J. G., Ciais, P., Jackson, R. B., Alin, S. R., Alkama, R., Arneth, A., Arora, V. K., Bates, N. R., Becker, M., Bellouin, N., Bittig, H. C., Bopp, L., Chevallier, F., Chini, L. P., Cronin, M., Evans, W., Falk, S., Feely, R. A., Gasser, T., Gehlen, M., Gkritzalis, T., Gloege, L., Grassi, G., Gruber, N., Gürses, O., Harris, I., Hefner, M., Houghton, R. A., Hurtt, G. C., Iida, Y., Ilyina, T., Jain, A. K., Jersild, A., Kadono, K., Kato, E., Kennedy, D., Klein Goldewijk, K., Knauer, J., Korsbakken, J. I., Landschützer, P., Lefèvre, N., Lindsay, K., Liu, J., Liu, Z., Marland, G., Mayot, N., McGrath, M. J., Metzl, N., Monacci, N. M., Munro, D. R., Nakaoka, S.-I., Niwa, Y., O'Brien, K., Ono, T., Palmer, P. I., Pan, N., Pierrot, D., Pocock, K., Poulter, B., Resplandy, L., Robertson, E., Rödenbeck, C., Rodriguez, C., Rosan, T. M., Schwinger, J., Séférian, R., Shutler, J. D., Skjelvan, I., Steinhoff, T., Sun, Q., Sutton, A. J., Sweeney, C., Takao, S., Tanhua, T., Tans, P. P., Tian, X., Tian, H., Tilbrook, B., Tsujino, H., Tubiello, F., van der Werf, G. R., Walker, A. P., Wanninkhof, R., Whitehead, C., Willstrand Wranne, A., Wright, R., Yuan, W., Yue, C., Yue, X., Zaehle, S., Zeng, J., and Zheng, B.: Global Carbon Budget 2022, Earth System Science Data, 14, 4811–4900, https://doi.org/10.5194/essd-14-4811-2022, 2022.

Göckede, M., Michalak, A. M., Vickers, D., Turner, D. P., and Law, B. E.: Atmospheric inverse modeling to constrain regional-scale CO_2 budgets at high spatial and temporal resolution, Journal of Geophysical Research: Atmospheres, 115, D15 113, https://doi.org/10.1029/2009JD012257, 2010.

Gourdji, S. M., Hirsch, A. I., Mueller, K. L., Yadav, V., Andrews, A. E., and Michalak, A. M.: Regional-scale geostatistical inverse modeling of North American CO_2 fluxes: a synthetic data study, Atmospheric Chemistry and Physics, 10, 6151–6167, https://doi.org/10.5194/acp-10-6151-2010, 2010.

Gourdji, S. M., Mueller, K. L., Yadav, V., Huntzinger, D. N., Andrews, A. E., Trudeau, M., Petron, G., Nehrkorn, T., Eluszkiewicz, J., Henderson, J., Wen, D., Lin, J., Fischer, M., Sweeney, C., and Michalak, A. M.: North American CO_2 exchange: inter-comparison of modeled estimates with results from a fine-scale atmospheric inversion, Biogeosciences, 9, 457–475, https://doi.org/10.5194/bg-9-457-2012, 2012.

Guanter, L., Zhang, Y., Jung, M., Joiner, J., Voigt, M., Berry, J. A., Frankenberg, C., Huete, A. R., Zarco-Tejada, P., Lee, J.-E., Moran, M. S., Ponce-Campos, G., Beer, C., Camps-Valls, G., Buchmann, N., Gianelle, D., Klumpp, K., Cescatti, A., Baker, J. M., and Griffis, T. J.: Global and time-resolved monitoring of crop photosynthesis with chlorophyll fluorescence, Proceedings of the National Academy of Sciences, 111, E1327–E1333, https://doi.org/10.1073/pnas.1320008111, 2014.

Harris, I. C.: CRU JRA v2.3: A forcings dataset of gridded land surface blend of Climatic Research Unit (CRU) and Japanese reanalysis (JRA) data; Jan.1901 - Dec.2021, https://catalogue.ceda.ac.uk/uuid/38715b12b22043118a208acd61771917/, 2022.

Held, I. M., Lyons, S. W., and Nigam, S.: Transients and the extratropical response to El Niño, Journal of Atmospheric Sciences, 46, 163–174, https://doi.org/10.1175/1520-0469(1989)046<0163:TATERT>2.0.CO;2, 1989.

Hoell, A., Hoerling, M., Eischeid, J., Wolter, K., Dole, R., Perlwitz, J., Xu, T., and Cheng, L.: Does El Niño intensity matter for California precipitation?, Geophysical Research Letters, 43, 819–825, https://doi.org/10.1002/2015GL067102, 2016.

Horel, J. D. and Wallace, J. M.: Planetary-scale atmospheric phenomena associated with the Southern Oscillation, Monthly Weather Review, 109, 813–829, https://doi.org/10.1175/1520-0493(1981)109<0813:PSAPAW>2.0.CO;2, 1981.

Hu, L., Andrews, A. E., Thoning, K. W., Sweeney, C., Miller, J. B., Michalak, A. M., Dlugokencky, E., Tans, P. P., Shiga, Y. P., Mountain, M., Nehrkorn, T., Montzka, S. A., McKain, K., Kofler, J., Trudeau, M., Michel, S. E., Biraud, S. C., Fischer, M. L., Worthy, D. E. J., Vaughn, B. H., White, J. W. C., Yadav, V., Basu, S., and van der Velde, I. R.: Enhanced North American carbon uptake associated with El Niño, Science Advances, 5, eaaw0076, https://doi.org/10.1126/sciadv.aaw0076, 2019.

Huang, B., Thorne, P. W., Banzon, V. F., Boyer, T., Chepurin, G., Lawrimore, J. H., Menne, M. J., Smith, T. M., Vose, R. S., and Zhang, H.-M.: NOAA Extended Reconstructed Sea Surface Temperature (ERSST), Version 5, https://doi.org/10.7289/V5T72FNM, 2017a.

Huang, B., Thorne, P. W., Banzon, V. F., Boyer, T., Chepurin, G., Lawrimore, J. H., Menne, M. J., Smith, T. M., Vose, R. S., and Zhang, H.-M.: Extended Reconstructed Sea Surface Temperature, Version 5 (ERSSTv5): Upgrades, validations, and intercomparisons, Journal of Climate, 30, 8179–8205, https://doi.org/10.1175/jcli-d-16-0836.1, 2017b.

Joiner, J., Yoshida, Y., Vasilkov, A. P., Yoshida, Y., Corp, L. A., and Middleton, E. M.: First observations of global and seasonal terrestrial chlorophyll fluorescence from space, Biogeosciences, 8, 637–651, https://doi.org/10.5194/bg-8-637-2011, 2011.

Joiner, J., Guanter, L., Lindstrot, R., Voigt, M., Vasilkov, A. P., Middleton, E. M., Huemmrich, K. F., Yoshida, Y., and Frankenberg, C.: Global monitoring of terrestrial chlorophyll fluorescence from moderate-spectral-resolution near-infrared satellite measurements: methodology, simulations, and application to GOME-2, Atmospheric Measurement Techniques, 6, 2803–2823, https://doi.org/10.5194/amt-6-2803-2013, 2013.

Jones, C. D. and Cox, P. M.: On the significance of atmospheric CO_2 growth rate anomalies in 2002–2003, Geophysical Research Letters, 32, L14 816, https://doi.org/10.1029/2005GL023027, 2005.

Jones, C. D., Collins, M., Cox, P. M., and Spall, S. A.: The carbon cycle response to ENSO: A coupled climate–carbon cycle model study, Journal of Climate, 14, 4113–4129, https://doi.org/10.1175/1520-0442(2001)014<4113:TCCRTE>2.0.CO;2, 2001.

Jong, B.-T., Ting, M., and Seager, R.: El Niño's impact on California precipitation: seasonality, regionality, and El Niño intensity, Environmental Research Letters, 11, 054 021, https://doi.org/10.1088/1748-9326/11/5/054021, 2016.

Jong, B.-T., Ting, M., Seager, R., and Anderson, W. B.: ENSO teleconnections and impacts on U.S. summertime temperature during a multiyear La Niña life cycle, Journal of Climate, 33, 6009 – 6024, https://doi.org/10.1175/jcli-d-19-0701.1, 2020.

Jong, B.-T., Ting, M., and Seager, R.: Assessing ENSO summer teleconnections, impacts, and predictability in North America, Journal of Climate, 34, 3629–3643, https://doi.org/10.1175/jcli-d-20-0761.1, 2021.

Keel, T.: Thomasjkeel/jsmetrics: 0.2.7, https://doi.org/10.5281/zenodo.13834517, https://doi.org/10.5281/zenodo.13834517, 2024.

Keel, T., Brierley, C., and Edwards, T.: jsmetrics v0.2.0: a Python package for metrics and algorithms used to identify or characterise atmospheric jet streams, Geoscientific Model Development, 17, 1229–1247, https://doi.org/10.5194/gmd-17-1229-2024, 2024.

Keeling, C. D., Whorf, T. P., Wahlen, M., and van der Plichtt, J.: Interannual extremes in the rate of rise of atmospheric carbon dioxide since 1980, Nature, 375, 666–670, https://doi.org/10.1038/375666a0, 1995.

Kobayashi, S., Ota, Y., Harada, Y., Ebita, A., Moriya, M., Onoda, H., Onogi, K., Kamahori, H., Kobayashi, C., Endo, H., Miyaoka, K., and Takahashi, K.: The JRA-55 reanalysis: General specifications and basic characteristics, Journal of the Meteorological Society of Japan, 93, 5–48, https://doi.org/10.2151/jmsj.2015-001, 2015.

Koren, G., van Schaik, E., Araújo, A. C., Boersma, K. F., Gärtner, A., Killaars, L., Kooreman, M. L., Kruijt, B., van der Laan-Luijkx, I. T., von Randow, C., Smith, N. E., and Peters, W.: Widespread reduction in sun-induced fluorescence from the Amazon during the 2015/2016 El Niño, Philosophical Transactions of the Royal Society B: Biological Sciences, 373, 20170 408, https://doi.org/10.1098/rstb.2017.0408, 2018.

Krishnamurthy, L., Vecchi, G. A., Msadek, R., Wittenberg, A., Delworth, T. L., and Zeng, F.: The seasonality of the Great Plains Low-Level Jet and ENSO relationship, Journal of Climate, 28, 4525–4544, https://doi.org/10.1175/jcli-d-14-00590.1, 2015.

Kumar, A. and Hoerling, M. P.: The nature and causes for the delayed atmospheric response to El Niño, Journal of Climate, 16, 1391–1403, https://doi.org/10.1175/1520-0442(2003)16<1391:TNACFT>2.0.CO;2, 2003.

Kurtzman, D. and Scanlon, B. R.: El Niño–Southern Oscillation and Pacific Decadal Oscillation impacts on precipitation in the southern and central United States: Evaluation of spatial distribution and predictions, Water Resources Research, 43, W10 427, https://doi.org/10.1029/2007WR005863, 2007.

Lee, S.-K., Lopez, H., Chung, E.-S., DiNezio, P., Yeh, S.-W., and Wittenberg, A. T.: On the fragile relationship between El Niño and California rainfall, Geophysical Research Letters, 45, 907–915, https://doi.org/10.1002/2017GL076197, 2018.

L'Heureux, M. L., Tippett, M. K., and Barnston, A. G.: Characterizing ENSO coupled variability and its impact on North American seasonal precipitation and temperature, Journal of Climate, 28, 4231–4245, https://doi.org/10.1175/JCLI-D-14-00508.1, 2015.

Li, N., Sippel, S., Linscheid, N., Rödenbeck, C., Winkler, A. J., Reichstein, M., Mahecha, M. D., and Bastos, A.: Enhanced global carbon cycle sensitivity to tropical temperature linked to internal climate variability, Science Advances, 10, eadl6155, https://doi.org/10.1126/sciadv.adl6155, 2024.

Liang, Y.-C., Yu, J.-Y., Lo, M.-H., and Wang, C.: The changing influence of El Niño on the Great Plains low-level jet, Atmospheric Science Letters, 16, 512–517, https://doi.org/10.1002/asl.590, 2015.

Lin, J. C., Gerbig, C., Wofsy, S. C., Andrews, A. E., Daube, B. C., Davis, K. J., and Grainger, C. A.: A near-field tool for simulating the upstream influence of atmospheric observations: The Stochastic Time-Inverted Lagrangian Transport (STILT) model, Journal of Geophysical Research: Atmospheres, 108, 4493, https://doi.org/10.1029/2002JD003161, 2003.

Lindsey, R.: In Watching for El Niño and La Niña, NOAA Adapts to Global Warming, https://www.climate.gov/news-features/understanding-climate/watching-el-ni%C3%B1o-and-la-ni%C3%B1a-noaa-adapts-global-warming, (Retrieved 2023-07-28), 2013.

Liu, J., Bowman, K. W., Schimel, D. S., Parazoo, N. C., Jiang, Z., Lee, M., Bloom, A. A., Wunch, D., Frankenberg, C., Sun, Y., O'Dell, C. W., Gurney, K. R., Menemenlis, D., Gierach, M., Crisp, D., and Eldering, A.: Contrasting carbon cycle responses of the tropical continents to the 2015–2016 El Niño, Science, 358, eaam5690, https://doi.org/10.1126/science.aam5690, 2017.

Liu, J., Baker, D., Basu, S., Bowman, K., Byrne, B., Chevallier, F., He, W., Jiang, F., Johnson, M. S., Kubar, T. L., Li, X., Liu, Z., Miller, S. M., Philip, S., Xiao, J., Yun, J., and Zeng, N.: The reduced net carbon uptake over Northern Hemisphere land causes the close-to-normal CO_2 growth rate in 2021 La Niña, Science Advances, 10, eadl2201, https://doi.org/10.1126/sciadv.adl2201, 2024.

Luna-Niño, R., Gershunov, A., Ralph, F. M., Weyant, A., Guirguis, K., DeFlorio, M. J., Cayan, D. R., and Williams, A. P.: Heresy in ENSO teleconnections: Atmospheric rivers as disruptors of canonical seasonal precipitation anomalies in the Southwestern US, Climate Dynamics, 63, https://doi.org/10.1007/s00382-025-07583-1, 2025.

Luo, X. and Keenan, T. F.: Tropical extreme droughts drive long-term increase in atmospheric CO_2 growth rate variability, Nature Communications, 13, https://doi.org/10.1038/s41467-022-28824-5, 2022.

Luo, X., Keenan, T. F., Fisher, J. B., Jiménez-Muñoz, J.-C., Chen, J. M., Jiang, C., Ju, W., Perakalapudi, N.-V., Ryu, Y., and Tadić, J. M.: The impact of the 2015/2016 El Niño on global photosynthesis using satellite remote sensing, Philosophical Transactions of the Royal Society B: Biological Sciences, 373, 20170 409, https://doi.org/10.1098/rstb.2017.0409, 2018.

Manney, G. L., Hegglin, M. I., Daffer, W. H., Santee, M. L., Ray, E. A., Pawson, S., Schwartz, M. J., Boone, C. D., Froidevaux, L., Livesey, N. J., Read, W. G., and Walker, K. A.: Jet characterization in the upper troposphere/lower stratosphere (UTLS): applications to climatology and transport studies, Atmospheric Chemistry and Physics, 11, 6115–6137, https://doi.org/10.5194/acp-11-6115-2011, 2011.

Masarie, K. A., Peters, W., Jacobson, A. R., and Tans, P. P.: ObsPack: A framework for the preparation, delivery, and attribution of atmospheric greenhouse gas measurements, Earth System Science Data, 6, 375–384, https://doi.org/10.5194/essd-6-375-2014, 2014.

McPhaden, M. J., Zebiak, S. E., and Glantz, M. H.: ENSO as an integrating concept in earth science, Science, 314, 1740–1745, https://doi.org/10.1126/science.1132588, 2006.

Mesinger, F., DiMego, G., Kalnay, E., Mitchell, K., Shafran, P. C., Ebisuzaki, W., Jović, D., Woollen, J., Rogers, E., Berbery, E. H., Ek, M. B., Fan, Y., Grumbine, R., Higgins, W., Li, H., Lin, Y., Manikin, G., Parrish, D., and Shi, W.: North American Regional Reanalysis, Bulletin of the American Meteorological Society, 87, 343–360, https://doi.org/10.1175/BAMS-87-3-343, 2006.

Michalak, A. M., Bruhwiler, L., and Tans, P. P.: A geostatistical approach to surface flux estimation of atmospheric trace gases, Journal of Geophysical Research: Atmospheres, 109, D14 109, https://doi.org/10.1029/2003JD004422, 2004.

Miller, S. M., Michalak, A. M., Yadav, V., and Tadić, J. M.: Characterizing biospheric carbon balance using CO_2 observations from the OCO-2 satellite, Atmospheric Chemistry and Physics, 18, 6785–6799, https://doi.org/10.5194/acp-18-6785-2018, 2018.

Mueller, K. L., Gourdji, S. M., and Michalak, A. M.: Global monthly averaged CO_2 fluxes recovered using a geostatistical inverse modeling approach: 1. Results using atmospheric measurements, Journal of Geophysical Research: Atmospheres, 113, D21114, https://doi.org/10.1029/2007JD009734, 2008.

Nehrkorn, T., Eluszkiewicz, J., Wofsy, S. C., Lin, J. C., Gerbig, C., Longo, M., and Freitas, S.: Coupled Weather Research and Forecasting–Stochastic Time-Inverted Lagrangian Transport (WRF–STILT) model, Meteorology and Atmospheric Physics, 107, 51–64, https://doi.org/10.1007/s00703-010-0068-x, 2010.

Nelson, J. A., Walther, S., Gans, F., Kraft, B., Weber, U., Novick, K., Buchmann, N., Migliavacca, M., Wohlfahrt, G., Šigut, L., Ibrom, A., Papale, D., Göckede, M., Duveiller, G., Knohl, A., Hörtnagl, L., Scott, R. L., Dušek, J., Zhang, W., Hamdi, Z. M., Reichstein, M., Aranda-Barranco, S., Ardö, J., Op de Beeck, M., Billesbach, D., Bowling, D., Bracho, R., Brümmer, C., Camps-Valls, G., Chen, S., Cleverly, J. R., Desai, A., Dong, G., El-Madany, T. S., Euskirchen, E. S., Feigenwinter, I., Galvagno, M., Gerosa, G. A., Gielen, B., Goded, I., Goslee, S., Gough, C. M., Heinesch, B., Ichii, K., Jackowicz-Korczynski, M. A., Klosterhalfen, A., Knox, S., Kobayashi, H., Kohonen, K.-M., Korkiakoski, M., Mammarella, I., Gharun, M., Marzuoli, R., Matamala, R., Metzger, S., Montagnani, L., Nicolini, G., O'Halloran, T., Ourcival, J.-M., Peichl, M., Pendall, E., Ruiz Reverter, B., Roland, M., Sabbatini, S., Sachs, T., Schmidt, M., Schwalm, C. R., Shekhar, A., Silberstein, R., Silveira, M. L., Spano, D., Tagesson, T., Tramontana, G., Trotta, C., Turco, F., Vesala, T., Vincke, C., Vitale, D., Vivoni, E. R., Wang, Y., Woodgate, W., Yepez, E. A., Zhang, J., Zona, D., and Jung, M.: X-BASE: the first terrestrial carbon and water flux products from an extended data-driven scaling framework, FLUXCOM-X, Biogeosciences, 21, 5079–5115, https://doi.org/10.5194/bg-21-5079-2024, 2024.

NOAA National Weather Service Climate Prediction Center: Oceanic Niño Index., https://origin.cpc.ncep.noaa.gov/products/analysis_monitoring/ensostuff/ONI_v5.php, retrieved 2024-07-12 from https://origin.cpc.ncep.noaa.gov/products/analysis_monitoring/ensostuff/ONI_v5.php, 2024a.

NOAA National Weather Service Climate Prediction Center: Monthly teleconnections products., https://www.cpc.ncep.noaa.gov/products/precip/CWlink/daily_ao_index/teleconnections.shtml, retrieved 2024-07-04 from https://www.cpc.ncep.noaa.gov/products/precip/CWlink/daily_ao_index/teleconnections.shtml, 2024b.

Page, S. E., Siegert, F., Rieley, J. O., Boehm, H.-D. V., Jaya, A., and Limin, S.: The amount of carbon released from peat and forest fires in Indonesia during 1997, Nature, 420, 61–65, https://doi.org/10.1038/nature01131, 2002.

Parazoo, N. C., Barnes, E., Worden, J., Harper, A. B., Bowman, K. B., Frankenberg, C., Wolf, S., Litvak, M., and Keenan, T. F.: Influence of ENSO and the NAO on terrestrial carbon uptake in the Texas-northern Mexico region, Global Biogeochemical Cycles, 29, 1247–1265, https://doi.org/10.1002/2015GB005125, 2015.

Pedregosa, F., Varoquaux, G., Gramfort, A., Michel, V., Thirion, B., Grisel, O., Blondel, M., Prettenhofer, P., Weiss, R., Dubourg, V., Vanderplas, J., Passos, A., Cournapeau, D., Brucher, M., Perrot, M., and Duchesnay, É.: Scikit-learn: machine learning in Python, Journal of Machine Learning Research, 12, 2825–2830, http://jmlr.org/papers/v12/pedregosa11a.html, 2011.

Porcar-Castell, A., Malenovský, Z., Magney, T., Van Wittenberghe, S., Fernández-Marín, B., Maignan, F., Zhang, Y., Maseyk, K., Atherton, J., Albert, L. P., Robson, T. M., Zhao, F., Garcia-Plazaola, J.-I., Ensminger, I., Rajewicz, P. A., Grebe, S., Tikkanen, M., Kellner, J. R., Ihalainen, J. A., Rascher, U., and Logan, B.: Chlorophyll *a* fluorescence illuminates a path connecting plant molecular biology to Earth-system science, Nature Plants, 7, 998–1009, https://doi.org/10.1038/s41477-021-00980-4, 2021.

Qian, H., Joseph, R., and Zeng, N.: Response of the terrestrial carbon cycle to the El Niño–Southern Oscillation, Tellus B: Chemical and Physical Meteorology, https://doi.org/10.1111/j.1600-0889.2008.00360.x, 2008.

Randazzo, N. A., Michalak, A. M., and Desai, A. R.: Synoptic meteorology explains temperate forest carbon uptake, Journal of Geophysical Research: Biogeosciences, 125, e2019JG005 476, https://doi.org/10.1029/2019JG005476, e2019JG005476 2019JG005476, 2020.

Randerson, J. T., van der Werf, G. R., Giglio, L., Collatz, G. J., and Kasibhatla, P. S.: Global Fire Emissions Database, Version 4.1, https://doi.org/10.3334/ORNLDAAC/1293, 2018.

Rastogi, B., Miller, J. B., Trudeau, M., Andrews, A. E., Hu, L., Mountain, M., Nehrkorn, T., Baier, B., McKain, K., Mund, J., Guan, K., and Alden, C. B.: Evaluating consistency between total column CO_2 retrievals from OCO-2 and the in situ network over North America: implications for carbon flux estimation, Atmospheric Chemistry and Physics, 21, 14 385–14 401, https://doi.org/10.5194/acp-21-14385-2021, 2021.

Rayner, N. A., Parker, D. E., Horton, E. B., Folland, C. K., Alexander, L. V., Rowell, D. P., Kent, E. C., and Kaplan, A.: Global analyses of sea surface temperature, sea ice, and night marine air temperature since the late nineteenth century, Journal of Geophysical Research: Atmospheres, 108, 4407, https://doi.org/10.1029/2002JD002670, 2003.

Rigby, R. A. and Stasinopoulos, D. M.: Generalized Additive Models for Location, Scale and Shape, Journal of the Royal Statistical Society Series C: Applied Statistics, 54, 507–554, https://doi.org/10.1111/j.1467-9876.2005.00510.x, 2005.

Rödenbeck, C., Zaehle, S., Keeling, R., and Heimann, M.: History of El Niño impacts on the global carbon cycle 1957–2017: a quantification from atmospheric CO_2 data, Philosophical Transactions of the Royal Society B: Biological Sciences, 373, 20170 303, https://doi.org/10.1098/rstb.2017.0303, 2018.

Ropelewski, C. F. and Jones, P. D.: An extension of the Tahiti–Darwin Southern Oscillation Index, Monthly Weather Review, 115, 2161–2165, https://doi.org/10.1175/1520-0493(1987)115<2161:AEOTTS>2.0.CO;2, 1987.

Schwarz, G.: Estimating the dimension of a model, The Annals of Statistics, 6, 461–464, https://doi.org/10.1214/aos/1176344136, 1978.

Seager, R., Harnik, N., Robinson, W. A., Kushnir, Y., Ting, M., Huang, H.-P., and Velez, J.: Mechanisms of ENSO-forcing of hemispherically symmetric precipitation variability, Quarterly Journal of the Royal Meteorological Society, 131, 1501–1527, https://doi.org/10.1256/qj.04.96, 2005.

Seager, R., Lis, N., Feldman, J., Ting, M., Williams, A. P., Nakamura, J., Liu, H., and Henderson, N.: Whither the 100th meridian? The once and future physical and human geography of America's arid–humid divide. Part I: The story so far, Earth Interactions, 22, 1–22, https://doi.org/10.1175/ei-d-17-0011.1, 2018.

Shaw, T. A. and Miyawaki, O.: Fast upper-level jet stream winds get faster under climate change, Nature Climate Change, 14, 61–67, https://doi.org/10.1038/s41558-023-01884-1, 2023.

Shiga, Y. P., Michalak, A. M., Fang, Y., Schaefer, K., Andrews, A. E., Huntzinger, D. H., Schwalm, C. R., Thoning, K., and Wei, Y.: Forests dominate the interannual variability of the North American carbon sink, Environmental Research Letters, 13, 084 015, https://doi.org/10.1088/1748-9326/aad505, 2018a.

Shiga, Y. P., Tadić, J. M., Qiu, X., Yadav, V., Andrews, A. E., Berry, J. A., and Michalak, A. M.: Atmospheric CO_2 observations reveal strong correlation between regional net biospheric carbon uptake and solar-induced chlorophyll fluorescence, Geophysical Research Letters, 45, 1122–1132, https://doi.org/10.1002/2017GL076630, 2018b.

Sitch, S., Friedlingstein, P., Gruber, N., Jones, S. D., Murray-Tortarolo, G., Ahlström, A., Doney, S. C., Graven, H., Heinze, C., Huntingford, C., Levis, S., Levy, P. E., Lomas, M., Poulter, B., Viovy, N., Zaehle, S., Zeng, N., Arneth, A., Bonan, G., Bopp, L., Canadell, J. G., Chevallier, F., Ciais, P., Ellis, R., Gloor, M., Peylin, P., Piao, S. L., Le Quéré, C., Smith, B., Zhu, Z., and Myneni, R.:

https://doi.org/10.5194/egusphere-2026-880
Preprint. Discussion started: 13 April 2026

Recent trends and drivers of regional sources and sinks of carbon dioxide, Biogeosciences, 12, 653–679, https://doi.org/10.5194/bg-12-653-2015, 2015.

Sitch, S., O'Sullivan, M., Robertson, E., Friedlingstein, P., Albergel, C., Anthoni, P., Arneth, A., Arora, V. K., Bastos, A., Bastrikov, V., Bellouin, N., Canadell, J. G., Chini, L., Ciais, P., Falk, S., Harris, I., Hurtt, G., Ito, A., Jain, A. K., Jones, M. W., Joos, F., Kato, E., Kennedy, D., Klein Goldewijk, K., Kluzek, E., Knauer, J., Lawrence, P. J., Lombardozzi, D., Melton, J. R., Nabel, J. E. M. S., Pan, N., Peylin, P., Pongratz, J., Poulter, B., Rosan, T. M., Sun, Q., Tian, H., Walker, A. P., Weber, U., Yuan, W., Yue, X., and Zaehle, S.: Trends and drivers of terrestrial sources and sinks of carbon dioxide: an overview of the TRENDY Project, Global Biogeochemical Cycles, 38, e2024GB008 102, https://doi.org/10.1029/2024GB008102, 2024.

Skamarock, W. C. and Klemp, J. B.: A time-split nonhydrostatic atmospheric model for weather research and forecasting applications, Journal of Computational Physics, 227, 3465–3485, https://doi.org/10.1016/j.jcp.2007.01.037, 2008.

Stagge, J. H., Torbenson, M. C. A., Sung, K., Phillips, B., and Kingston, D. G.: Orographic amplification of El Niño teleconnections on winter precipitation across the Intermountain West of North America, Nature Water, 1, 1016–1026, https://doi.org/10.1038/s44221-023-00163-9, 2023.

Stensrud, D. J.: Importance of low-level jets to climate: A review, Journal of Climate, 9, 1698–1711, https://doi.org/10.1175/1520-0442(1996)009<1698:IOLLJT>2.0.CO;2, 1996.

Su, H., Neelin, J. D., and Meyerson, J. E.: Mechanisms for lagged atmospheric response to ENSO SST forcing, Journal of Climate, 18, 4195–4215, https://doi.org/10.1175/jcli3514.1, 2005.

Sun, W., Fang, Y., Luo, X., Shiga, Y. P., Zhang, Y., Andrews, A. E., Thoning, K. W., Fisher, J. B., Keenan, T. F., and Michalak, A. M.: Midwest US croplands determine model divergence in North American carbon fluxes, AGU Advances, 2, e2020AV000 310, https://doi.org/10.1029/2020AV000310, 2021.

Sun, Y., Frankenberg, C., Wood, J. D., Schimel, D. S., Jung, M., Guanter, L., Drewry, D. T., Verma, M., Porcar-Castell, A., Griffis, T. J., Gu, L., Magney, T. S., Köhler, P., Evans, B., and Yuen, K.: OCO-2 advances photosynthesis observation from space via solar-induced chlorophyll fluorescence, Science, 358, eaam5747, https://doi.org/10.1126/science.aam5747, 2017.

Tadić, J. M., Qiu, X., Miller, S., and Michalak, A. M.: Spatio-temporal approach to moving window block kriging of satellite data v1.0, Geoscientific Model Development, 10, 709–720, https://doi.org/10.5194/gmd-10-709-2017, 2017.

Trenberth, K. E., Branstator, G. W., Karoly, D., Kumar, A., Lau, N.-C., and Ropelewski, C.: Progress during TOGA in understanding and modeling global teleconnections associated with tropical sea surface temperatures, Journal of Geophysical Research: Oceans, 103, 14 291–14 324, https://doi.org/10.1029/97JC01444, 1998.

van der Werf, G. R., Randerson, J. T., Collatz, G. J., Giglio, L., Kasibhatla, P. S., Arellano, A. F., Olsen, S. C., and Kasischke, E. S.: Continental-Scale Partitioning of Fire Emissions During the 1997 to 2001 El Niño/La Niña Period, Science, 303, 73–76, https://doi.org/10.1126/science.1090753, 2004.

van der Werf, G. R., Randerson, J. T., Giglio, L., van Leeuwen, T. T., Chen, Y., Rogers, B. M., Mu, M., van Marle, M. J. E., Morton, D. C., Collatz, G. J., Yokelson, R. J., and Kasibhatla, P. S.: Global fire emissions estimates during 1997–2016, Earth System Science Data, 9, 697–720, https://doi.org/10.5194/essd-9-697-2017, 2017.

Wang, W., Ciais, P., Nemani, R. R., Canadell, J. G., Piao, S., Sitch, S., White, M. A., Hashimoto, H., Milesi, C., and Myneni, R. B.: Variations in atmospheric CO_2 growth rates coupled with tropical temperature, Proceedings of the National Academy of Sciences, 110, 13 061–13 066, https://doi.org/10.1073/pnas.1219683110, 2013.

Wang, X., Piao, S., Ciais, P., Friedlingstein, P., Myneni, R. B., Cox, P., Heimann, M., Miller, J., Peng, S., Wang, T., Yang, H., and Chen, A.: A two-fold increase of carbon cycle sensitivity to tropical temperature variations, Nature, 506, 212–215, https://doi.org/10.1038/nature12915, 2014.

Wolf, S., Keenan, T. F., Fisher, J. B., Baldocchi, D. D., Desai, A. R., Richardson, A. D., Scott, R. L., Law, B. E., Litvak, M. E., Brunsell, N. A., Peters, W., and van der Laan-Luijkx, I. T.: Warm spring reduced carbon cycle impact of the 2012 US summer drought, Proceedings of the National Academy of Sciences, 113, 5880–5885, https://doi.org/10.1073/pnas.1519620113, 2016.

Wolter, K. and Timlin, M. S.: Monitoring ENSO in COADS with a seasonally adjusted principal component index, in: Proceedings of the 17th Climate Diagnostics Workshop., pp. 52–57, NOAA/NMC/CAC, NSSL, Oklahoma Climatological Survey, CIMMS and the School of Meteorology, University of Oklahoma, Norman, OK, USA, https://www.psl.noaa.gov/enso/mei.old/WT1.pdf, retrieved 2023-07-29 from https://www.psl.noaa.gov/enso/mei.old/WT1.pdf, 1993.

Yadav, V. and Michalak, A. M.: Improving computational efficiency in large linear inverse problems: an example from carbon dioxide flux estimation, Geoscientific Model Development, 6, 583–590, https://doi.org/10.5194/gmd-6-583-2013, 2013.

Yadav, V., Mueller, K. L., and Michalak, A. M.: A backward elimination discrete optimization algorithm for model selection in spatio-temporal regression models, Environmental Modelling & Software, 42, 88–98, https://doi.org/10.1016/j.envsoft.2012.12.009, 2013.

Zhang, T., Hoell, A., Perlwitz, J., Eischeid, J., Murray, D., Hoerling, M., and Hamill, T. M.: Towards probabilistic multivariate ENSO monitoring, Geophysical Research Letters, 46, 10 532–10 540, https://doi.org/10.1029/2019GL083946, 2019a.

Zhang, Y., Dannenberg, M. P., Hwang, T., and Song, C.: El Niño–Southern Oscillation-induced variability of terrestrial gross primary production during the satellite era, Journal of Geophysical Research: Biogeosciences, 124, 2419–2431, https://doi.org/10.1029/2019JG005117, 2019b.

Zomer, R. J., Xu, J., and Trabucco, A.: Version 3 of the Global Aridity Index and Potential Evapotranspiration Database, Scientific Data, 9, https://doi.org/10.1038/s41597-022-01493-1, 2022.